Document Version
Final published version

Citation (APA)
Li, Z., Fan, J., & Zhang, G. (2026). A new physics-motivated constitutive model of hyperelastic polymer networks. *International Journal of Mechanical Sciences*, *314*, Article 111366. https://doi.org/10.1016/j.ijmecsci.2026.111366

International Journal of Mechanical Sciences 314 (2026) 111366

Contents lists available at ScienceDirect

International Journal of Mechanical Sciences

journal homepage: www.elsevier.com/locate/ijmecsci

A new physics-motivated constitutive model of hyperelastic polymer networks

Zichuan Li [a], Jiajie Fan [a,b], Guoqi Zhang [a,*]

[a] *Department of Microelectronics, Delft University of Technology, Delft, 2628 CD, The Netherlands*

[b] *College of Intelligent Robotics and Advanced Manufacturing, Fudan University, Shanghai, 200433, PR China*

ARTICLE INFO

Keywords:
Hyperelasticity
Constitutive model
Polymer network
Inverse Langevin chain statistics
Micro–macro mapping
General invariant

ABSTRACT

This study is motivated by a conceptual inconsistency in the physical interpretation of eight-chain hyperelastic theory, which arises from the combined effect of two distinct issues: the use of the marginal projection distribution $p_z(|r_z|)$ as a surrogate for the full probability density of end-to-end distance $p_{\bar{r}}(\bar{r})$, and the subsequent reliance on a root mean square (RMS) approximation step in the micro–macro averaging of chain stretch. We first revisit this probabilistic mismatch by reformulating the probability density function of freely-jointed chains (FJCs) in terms of the squared end-to-end vector $\boldsymbol{r}^2$, thereby restoring consistency on chain-level statistics. Building on this formulation, the micro–macro mapping averaging of chain conformational free energy is constructed directly in terms of $\boldsymbol{r}^2$, leading to a one-step mean-field approximation that avoids RMS averaging. The modified probability transformation is examined by Monte Carlo sampling at the microscopic level. To account for interchain interactions, q-mean statistical description of micro tube confinement was incorporated, leading to the appearance of the general invariant $I_q = \lambda_1^q + \lambda_2^q + \lambda_3^q$. The resulting continuum constitutive model is assessed against multiaxial experimental data for several polymer networks, including vulcanized natural rubber, Entec Enflex S4035A thermoplastic elastomer, Tetra-PEG, and isoprene rubber vulcanizate. Comparisons with three existing hyperelastic strain energy formulations, the extended eight-chain, extended tube models, and the four-parameter "comprehensive" model, demonstrate comparable phenomenological accuracy of the current model while providing a clearer and more consistent micro–macro physical interpretation of model parameters. A parametric study further illustrates how the dimensionless parameters n and q govern the shape of the macroscopic stress–strain responses. The present formulation provides a consistent theoretical basis within the scope of hyperelasticity and admits potential extensions toward more complex irreversible phenomena.

1. Introduction

Soft materials with polymeric networks are widely used in modern industries and are still attracting the interest of scientific communities. Emerging applications include, but are not limited to, flexible sensors [1], soft actuators [2], organ-on-a-chip [3], and wearable devices [4]. Among the various constitutive ingredients used to describe the mechanical behavior of such materials, the nonlinear elastic response under finite deformation plays a central role and is still an active topic within the realm of mechanical science. This elastic contribution is commonly represented through a hyperelastic strain–energy function. The major approaches to constructing the strain–energy function can be roughly classified into two categories: the phenomenological method and the physics-based method. In the first approach [5–10], functional forms are purely or mainly subjected to the constraints from continuum mechanics, e.g., frame indifference, second law of thermodynamics, material symmetry, etc., and the parameters do not clearly connect to molecular conformations. In contrast, physics-based models [11–16] start with a clear physical picture of the molecular conformation under assumptions from statistical physics and an assumed micro–macro network deformation mapping.

The eight-chain model proposed by Arruda and Boyce [13] was a milestone in the history of physics-based modeling of hyperelastic materials, for it captures general predictions via a more realistic microscopic physics picture of polymeric networks compared to earlier three-chain or four-chain models. Conceptually, the eight-chain model considered the bulk elastic free energy density as the inverse Langevin function of the ensemble average microstretch of freely-jointed chains (FJC). Their physical picture was further generalized

---

* Corresponding author.
E-mail address: G.Q.Zhang@tudelft.nl (G. Zhang).

https://doi.org/10.1016/j.ijmecsci.2026.111366
Received 17 September 2025; Received in revised form 26 January 2026; Accepted 7 February 2026

to a full network model soon [14,17]. In succession, various correction terms were introduced to the eight-chain model to improve the prediction of softening and hardening stages and complex multiaxial behaviors of soft materials. Bechir, et al. [18] reported a hybrid model with four parameters combining the three-chain model and the eight-chain model. Although they begin with a physics-based single-chain spring, the weights of contributions from the eight-chain network and the three-chain network are phenomenologically determined without clear physical explanation. Miehe and coworkers [19,20] proposed a micro-sphere model by introducing a tube constraint and a non-affine mapping between micro stretch and continuum deformation to the full network model [21] and presented a verification case with the finite element method (FEM). The microsphere model offers a clear physical picture and good phenomenological precision in predicting the complex multiaxial behavior of soft materials (see [22–25] for a detailed benchmark of early mainstream models up to 2023). Those advantages of the microsphere framework ensure its extendability to convert one-dimensional non-elastic models, for instance, anisotropic damage effects [26–28], phase transition [29], and general viscoplasticity, to three-dimensional cases. However, those models usually lack a universal closed-form on the continuum level and cause numerical complexity in simulation. In addition to the micro–macro mappings above, a few researchers [30,31] constructed the network picture in an alternative way, i.e., assuming equal force instead of directly connecting the macro-deformation to micro-stretches. However, the application of the equal force assumption is limited mainly by its mathematical complication.

Recently emerging experimental studies demonstrated that deliberately increasing entanglement density has become a prominent strategy for enhancing the mechanical properties of polymer networks [32–36]. This trend indicates that hyperelastic models should incorporate interchain entanglement through explicit elastic constraints, rather than subsuming its effects into phenomenological adjustments aimed at multiaxial fitting. The most widely used entanglement formulation is the tube model, first conceptualized by [37]. This idea was later extended to various continuum models, for instance, [38–40]. Among those derivatives of the tube model, a so-called slip-link model with four parameters derived from the tube model [15,16] successfully connects the macro parameters to molecular quantities. However, the application of the slip-link model was limited by its mathematical complications. Darabi and Itskov [41] generalized those historical tube models into a uniform functional form, which is considered a special case of the Ogden formulation. Notably, tube confinements introduced as standalone terms are inherently unable to capture the finite chain extensibility in the large-deformation regime, since they are formulated within a Gaussian statistical framework. The hybrid modeling combining the finite extensibility of cross-linked chains and the tube confinement has become a common practice to balance the physical meaning and phenomenological flexibility [42]. Kaliske and Heinrich [43] proposed a hybrid model that extends tube confinement by imposing an extendability coefficient to reproduce the asymptotic hardening of crosslinked chains without introducing non-Gaussian statistics. [44,45] presented a more non-Gaussian polymer network picture that integrates the eight-chain model with a three-tube topological confinement, which, in a manner similar to the physics picture in [46], achieves good agreement with several datasets of rubber-like materials. That model was further modified by a multi-well energy landscape of tube confinement to capture more complicated entanglement-dominant behaviors [47].

At the continuum level, both phenomenological and physics-based constitutive models necessarily admit invariant (or equivalently, eigenvalues of the deformation tensor for Valanis-Landel formulations [48, 49] and Ogden formulations [50]) representations in order to satisfy frame-indifference and material symmetry. The distinction between these two approaches does not lie in the use of invariants or the way to extract material constants, but in how the functional dependence on these invariants and eigenvalues is motivated and constructed. Phenomenological models thus enjoy a more flexible principle in constructing the specific functional form of strain energy and choosing invariant representations, albeit with an unfortunate trade-off in physical interpretability. Historically, the phenomenological methods (e.g., neo-Hookean, Mooney–Rivlin [51,52], Yeoh [6], Gent [5], Lopez-Pamies [53], etc.) chose the first and/or second invariants (I_1 and I_2) as the representations in the incompressible limit. Since any complete set of representations is mathematically equivalent to the combination of I_1 and I_2, the specific forms of those models depended mainly on the researchers' intuition about the experimental data. In recent years, efforts have been made to bridge the aforementioned gap between phenomenological and physics-based approaches. Gent model was initially proposed as a purely phenomenological model, but its molecular-statistical basis was then quantitatively discussed by [54–56]. Recently, Anssari-Benam [57] explicitly reached a strain energy function with a similar form to the Gent model by taking a rounded Padé approximation of the inverse Langevin function in micro-chain stretch. That model was then extended to more flexible semi-physics-based forms [58,59] by admitting the approximation index as an arbitrary positive material parameter or introducing a Pucci-Saccomandi-type correction term [60]. Within this phenomenological class, the state-of-the-art comprehensive model [61] is obtained by replacing the invariant arguments in the functional form of [58] with the Ogden-type generalized principal-stretch invariant $I_q = \lambda_1^q + \lambda_2^q + \lambda_3^q$. Although the model was subsequently assessed using broader experimental datasets [62,63] and extended to compressible regimes [64], its core functional form, devised by [58], partially lost a connection to physics and mathematical roots due to the aforementioned arbitrariness. Another approach to generalizing invariant representations is to choose the Landau invariants with an alternative deformation measurement [65].

The motivation of this study is our question regarding the two-step approximation, $\langle \psi_{FJC}(\bar{r}) \rangle \approx \psi_{FJC}(\langle \bar{r} \rangle) \approx \psi_{FJC}\left(\sqrt{\langle \boldsymbol{r} \cdot \boldsymbol{r} \rangle}\right)$, which is widely used in the aforementioned physics-based hyperelastic models, where ψ_{FJC} is the Helmholtz energy of a single FJC; $\boldsymbol{r}$ is so-called end-to-end vector of the FJC; symbol $\langle * \rangle$ denotes the mean value of quantities over the local ensemble. In Gaussian statistics, the approximation is absent, since the closed-form bulk strain energy density over the polymeric network can be analytically calculated by a Gaussian integral. In the non-Gaussian chain model, such an analytical operation becomes formidable, leading to the former approximation, known as a type of mean-field approximation, to achieve a closed-form bulk strain energy density. The latter approximation, i.e., root mean square (RMS) approximation, is introduced mainly to simplify the calculation of the mean end-to-end distance $\langle \bar{r} \rangle$. However, the accuracy of this approximation is questionable for a short chain ($n \approx 10$), which corresponds to the typical range of n fitted from highly crosslinked polymer networks. This deviation is not a numerical one, but rather the omission of the functional difference. Our proposition is to rewrite the entropy of the single FJC with a change of variable $u = \frac{\boldsymbol{r} \cdot \boldsymbol{r}}{(nb)^2}$ and provide the affine deformation assumption in an alternative form that connects the macro-deformation of material to the micro-stretch of u, so that the second approximation vanishes. In departure from the proposed entropy of the FJC model, we develop a simple physics-based model that consists of a full network picture and an entanglement contribution inspired by tube theory to improve the model's prediction of multiaxial behaviors. The proposed model has only four parameters. Within them, three are directly connected to microscopic quantities, and one is semi-empirically defined order of the power mean, encapsulating the complex non-affine micro–macro mapping and numerous intermolecular interactions that cause a deviation of the real network system from our ideal physical picture. The proposed model phenomenologically agrees well with various sets of materials while its parameters take physically meaningful values.

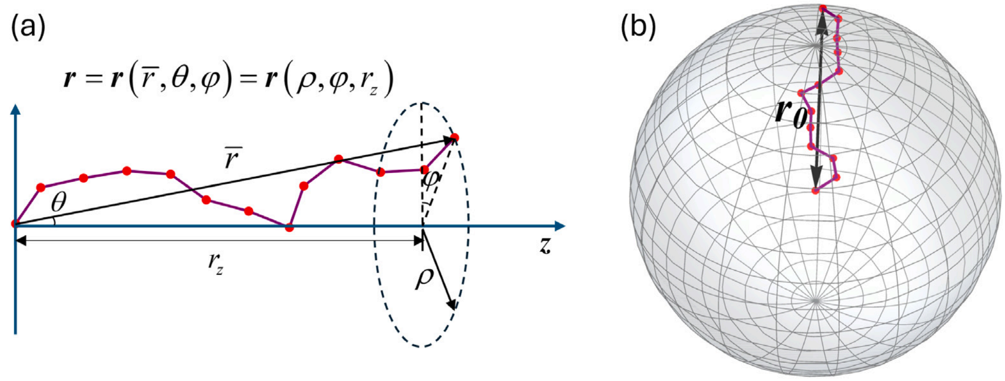

Fig. 1. Sketch of freely-jointed chains. (a) Illustration of a physical conformation of a freely-jointed chain with end-to-end vector $\boldsymbol{r}$ and the local cylindrical coordinate system. r_z measures the length of projection of $\boldsymbol{r}$ on the z–axis, and $\bar{r}$ represents the real end-to-end distance; (b) Isotropic directional probability density of chains in the undeformed polymer network.

The present manuscript is organized as follows: Section 2 gives an overall description of micro mechanics and the micro–macro mapping used in the current model. This section starts with a concise review of the classical FJC model, then derives and validates a new single-chain Helmholtz free energy function via a statistical approach. In addition, the interchain entanglements are taken into account via the tube-like free energy function. Both effects are linked to the macroscopic deformation via mean field averaging approaches. Section 3 further derives the explicit expressions of the continuum constitutive model with elementary functions through taking a reasonable approximation of the inverse Langevin function. Section 4 shows the validation of the proposed model with classical datasets of vulcanized rubbers, S4035A thermoplastic elastomers (TPE), Tetra-polyethylene glycol (PEG) gel, and isoprene rubber vulcanizate. A comparison with three other existing hyperelastic models and a parametric discussion on the current model are presented following the validation. Section 5 closes the paper with concluding remarks.

2. Microscopic description

The hyperelasticity of the polymer networks is also called entropic elasticity since it originates from the tendency of polymer chains to return to their maximum conformational entropy state upon deformation, driven by thermal fluctuations rather than energetic bond stretching. The cross-linked chains in the polymer network are stretched with the macroscopic deformation and suffer a decrease in the number of accessible conformational states. Besides, in a realistic polymer network, the entanglements with the surrounding chains have a significant contribution to the deviation of the eight-chain model from biaxial experiment data. In this section, we give an introduction to the mathematical descriptions of energy contributions from single-chain micro stretches and inter-chain entanglements.

2.1. Statistical description of FJC

The individual polymer chains in the network can be treated as nonlinear entropic springs. The model of the chain stretch part starts with finding an exact Helmholtz free energy function against the end-to-end length $\bar{r}$ of the polymer chains. A useful method is the freely-jointed chain model that assumes each chain has n freely-jointed rigid segments with identical length b, namely the Kuhn length [66]. A probability density of the end-to-end vector $\boldsymbol{r}$ of FJC with a projection r_z in an arbitrary direction $\boldsymbol{z}$ was proposed by [66]. Its expression is

$$p_z = C_0 \left(\frac{\sinh\beta}{\beta}\right)^n \exp\left(-\frac{\beta r_z}{b}\right), \quad \text{with } \beta = \mathcal{L}^{-1}\left(\frac{r_z}{nb}\right), \tag{1}$$

where $\mathcal{L}(*) = \coth(*) - \frac{1}{*}$ is the Langevin function and β is the inverse Langevin function against the normalized projection $r_z/(nb)$; C_0 is a normalization constant. Note that p_z in Eq. (1) captures the probability density of projection r_z instead of the end-to-end distance, which shall be magnitude of the end-to-end vector $\bar{r}$ as illustrated in Fig. 1a. That means using this probability density directly to calculate the entropy of three-dimensional FJC is questionable [67]. To solve this, we convert the marginal probability density of r_z to that of $\bar{r}$ in the next steps, since the directional distribution of the end-to-end vector is isotropic [68]. Setting a local cylindrical coordinate system, and the end-to-end vector of FJC is $\boldsymbol{r} = \boldsymbol{r}(\rho, \varphi, r_z)$. For the isotropic random walk, the probability density $p(\boldsymbol{r})$ has a simple relationship with the radial probability density in $\bar{r}$. That is

$$p(\boldsymbol{r}) = \frac{p_{\bar{r}}}{4\pi \bar{r}^2}, \tag{2}$$

and the probability density in projection r_z can be connected to $p_{\bar{r}}$ via a transform.

$$p_z = 2\pi \int_0^{\sqrt{n^2b^2-r_z^2}} p(\boldsymbol{r})\rho \, d\rho = 2\pi \int_{|r_z|}^{nb} p(\boldsymbol{r})\sqrt{\bar{r}^2 - r_z^2}\,\frac{d\rho}{d\bar{r}}\, d\bar{r} = \int_{|r_z|}^{nb} \frac{p_{\bar{r}}}{2\bar{r}}\, d\bar{r}, \tag{3}$$

According to Leibniz integral rule, differentiation with respect to the lower integration bound $|r_z|$ isolates the probability contribution from the spherical shell $\bar{r} = |r_z|$, thereby recovering the radial probability density of $p_{\bar{r}}$

$$p_{\bar{r}} = -2\bar{r}\left(\frac{dp_z}{dr_z}\right)_{r_z=\bar{r}}. \tag{4}$$

Worth mentioning that using Eq. (1) to compute the entropy variance induced by chain stretch causes a subtle conceptual mismatch in the physical picture of eight-chain models. That is, Eq. (1) predicts an entropically favorable conformation with zero end-to-end distance ($\bar{r} = 0$), which instead shall be one of the most unfavorable conformations of FJC as predicted by Eq. (4) and the Monte Carlo simulation (refer to Fig. A.15 for a visual comparison).

In most models with non-Gaussian statistics of FJC, for instance [13, 44,69], and those reviewed in [70], the mean-field approximation $\langle \psi_{FJC}(\bar{r})\rangle \approx \psi_{FJC}(\langle \bar{r}\rangle)$ is used to make macroscopic constitutive relationships analytically and computationally tractable. This approach has been proven effective and phenomenologically accurate for extensive cases. However, the following evaluation of free energy by substituting root mean square of $\bar{r}$ into the mean end-to-end distance (i.e., $\psi_{FJC}(\langle \bar{r}\rangle) \approx \psi_{FJC}\left(\sqrt{\langle \boldsymbol{r}\cdot\boldsymbol{r}\rangle}\right)$) is problematic. Mathematically, $\langle \boldsymbol{r}\cdot\boldsymbol{r}\rangle$ always convergences to nb^2 at a large number of FJCs, while $\langle \bar{r}\rangle$ does not. Fig. 2(a) shows a relative error of about 8% between them, which is caused by a structural difference between RMS and mean value thus cannot be eliminated by assuming an ensemble with a

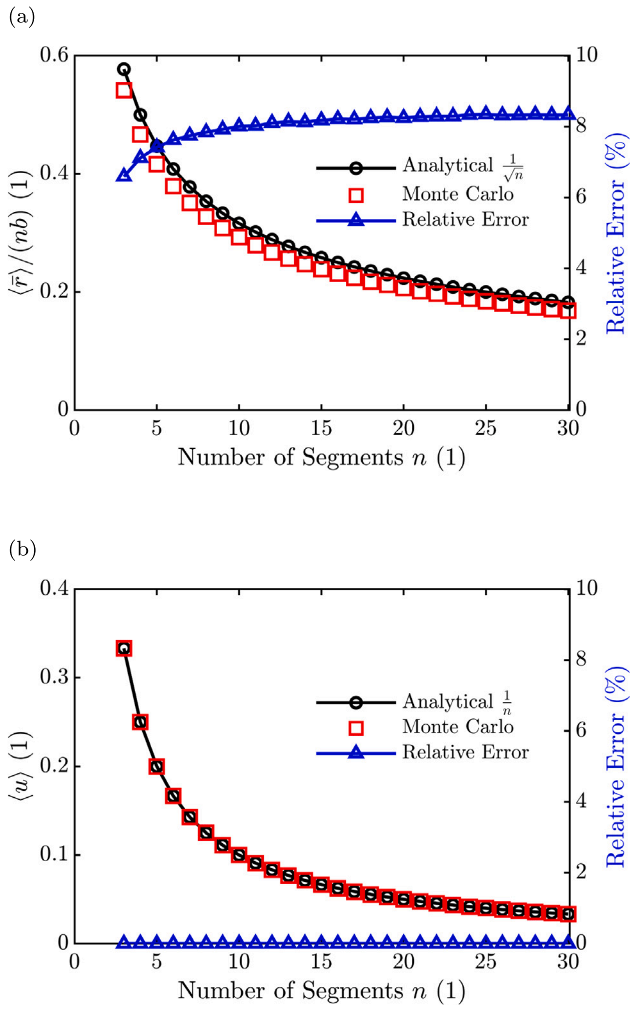

Fig. 2. Analytical calculation and corresponding relative errors of (a) the normalized mean end-to-end distance $\langle\bar{r}\rangle/(nb)$, and (b) normalized mean square of end-to-end distance $\langle u\rangle$. The Monte Carlo sampling accounts 10^7 independent chains. At this ensemble size, simulation results are highly stable.

large number of chains or of Kuhn segments. Moreover, the functional form of the single-chain free energy ψ_{FJC} derived from Eq. (1), which is widely used in eight-chain-type models, is itself problematic, as discussed above. To avoid this issue, we instead introduce the square of the normalized end-to-end distance u as the independent state variable

$$u(\bar{r}) := \frac{\boldsymbol{r}\cdot\boldsymbol{r}}{(nb)^2} = \left(\frac{\bar{r}}{nb}\right)^2, \tag{5}$$

to the derivation of constitutive relationships. As illustrated in Fig. 1a, the probability density of $u(\bar{r})$ shall be determined by that of $\bar{r}$ (Eq. (4)) rather than that of r_z (Eq. (1)). The mean value of u in an unstretched FJC can be properly evaluated via

$$\langle u_0\rangle = \frac{1}{n}, \tag{6}$$

since the segments are assumed fully independent in the FJC theory (see Fig. 2(b) for a numerical showcase). The probability density function of u preserves the relation

$$p_u(u) = p_{\bar{r}}(\bar{r}(u))\frac{d\bar{r}(u)}{du}, \tag{7}$$

since the probability density function of the end-to-end vector is orientation independent. The transformed probability density function of u is obtained by substituting Eqs. (1) and (4) into Eq. (7),

$$p_u = n^2 bC_0\beta\exp\left(-n\beta\sqrt{u}\right)\left(\frac{\sinh\beta}{\beta}\right)^n, \quad \text{with} \quad \beta = \mathcal{L}^{-1}\left(\sqrt{u}\right). \tag{8}$$

The validation of the probability density Eq. (8) was checked with the Monte Carlo sampling over an ensemble consisting of $N_{MC} = 10^7$ FJCs. Fig. 3(a) shows a significant deviation that is inherited from a defect of inverse Langevin chain theory, i.e., $n + \frac{1}{2} \approx n$ was assumed in the derivation of Eq. (1) [66], which leads to a structural inaccuracy for the chain with a short length (see also Fig. A.15a&b for the cases of p_r and p_z). Due to this nature, such a deviation decreases sharply with increasing number of segments. The values of n in Figs. 3(b) and 3(c) are taken from n of vulcanized natural rubber A and B, respectively, fitted by the current model. Fig. 3(b) shows acceptable deviations between Monte Carlo sampling and theoretical prediction of $\langle u\rangle$ even for the minimal fitted n value in this study, thus it indicates that Eq. (8) is sufficiently accurate for the following derivation of free energy function.

Considering that the conformational entropy of an individual FJC follows the Boltzmann equation $s = k_B \ln p_u$[71], the Helmholtz free energy of FJC is

$$\psi_{FJC}(u) = U_0 - k_B T \ln p_u, \tag{9}$$

where k_B is the Boltzmann constant; T is the absolute temperature; U_0 is a constant internal energy.

2.2. Stretch of cross-linked polymer network

Based on this modified statistical description of a single FJC, we are now able to access the deformation energy stored in the stretched polymer network. The macroscopic deformation can be connected to the micro-stretches of the FJC in the network by defining the following gyration-like second-order conformation tensor:

$$\boldsymbol{A} := \langle\boldsymbol{r}\otimes\boldsymbol{r}\rangle, \tag{10}$$

where $\otimes$ denotes the tensor product.

Notice that the average u can be directly related to the trace of the conformation tensor via the derivation below. Considering that the network contains N FJCs in unit volume, the conformation tensor $\boldsymbol{A}$ can be calculated from its definition:

$$\boldsymbol{A} = \frac{1}{N}\sum_{\alpha=1}^{N}\left(r_i^\alpha r_j^\alpha \boldsymbol{e}_i\otimes\boldsymbol{e}_j\right), \tag{11}$$

where $\boldsymbol{e}_i$, $\boldsymbol{e}_j$ are eigenvectors of $\boldsymbol{A}$; r_i^α, r_j^α are the projection of α-th end-to-end vector on eigenvectors; the Latine indices $i, j, \ldots \in \{1, 2, 3\}$ denote spatial coordinates and obey Einstein summation throughout this work. Taking the trace of (11),

$$\frac{tr(\boldsymbol{A})}{n^2b^2} = \frac{1}{N}\sum_{\alpha=1}^{N}\left(\frac{r_i^\alpha r_j^\alpha\delta_{ij}}{n^2b^2}\right) = \frac{1}{N}\sum_{\alpha=1}^{N}(u^\alpha) = \langle u\rangle, \tag{12}$$

where δ_{ij} is the Kronecker delta function.

For convenience, an affine deformation is assumed in the sense of the conformation tensor $\boldsymbol{A}$ instead of the end-to-end vector $\boldsymbol{r}$:

$$\boldsymbol{A} = \boldsymbol{F}\cdot\boldsymbol{A}_0\cdot\boldsymbol{F}^T, \tag{13}$$

where $\boldsymbol{F}$ is the continuum deformation gradient tensor; index 0 denotes the quantities in the cross-linking state. The assumption in Eq. (13) does not require but is compatible with the classical affine deformation assumption $\boldsymbol{r} = \boldsymbol{F}\cdot\boldsymbol{r}_0$. In undeformed reference polymer networks, the conformation tensor $\boldsymbol{A}_0$ is spherical

$$\boldsymbol{A}_0 = \frac{nb^2}{3}\boldsymbol{I}, \tag{14}$$

where $\boldsymbol{I}$ represents identity tensor. In this limit, the average micro-stretch degenerates to the widely used form $\langle\bar{\lambda}^2\rangle = \frac{I_1}{3n}$ with I_1 being

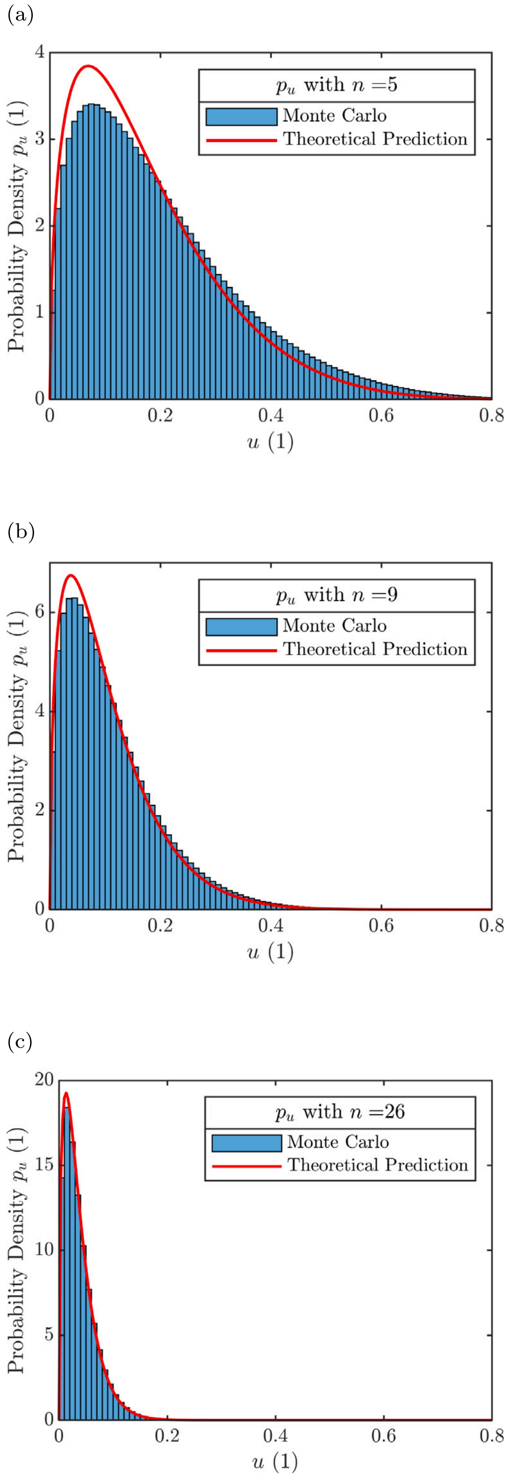

Fig. 3. Probability density predicted by Eq. (8) and Monte Carlo sampling of n-segment FJCs: (a) $n = 5$; (b) $n = 9$; (c) $n = 26$. The histogram contains 100 bins in total to achieve a smooth enough shape of the simulated probability density.

the first invariant (trace) of the right Cauchy–Green deformation tensor $\boldsymbol{C} = \boldsymbol{F}^T \cdot \boldsymbol{F}$. Note the fact that even though we assumed the polymer network is initially isotropic for the mathematical convenience of the following discussion, the relation (12) itself holds for FJC networks that consist of symmetric Kuhn segments under arbitrary anisotropic directional distribution. Therefore, the current modeling approach can be easily adapted to model the finite chain extendability in some special soft materials with anisotropic molecular conformation, such as liquid crystal elastomers [72,73] and biological tissues [74].

At the microscopic level, each polymer chain is assumed to be in thermodynamic equilibrium. The Helmholtz free energy density stored by the stretch of a cross-linked FJC network can be estimated by averaging the free energy of chains. In the sense of mean-field,

$$\mathcal{F}_s = N\langle \psi_{FJC}(u)\rangle \approx N\psi_{FJC}(\langle u\rangle). \tag{15}$$

2.3. *Tube-like constraint*

The inverse Langevin statistics-based models work well in explaining the hardening caused by the finite extensibility of the polymer network at the large deformation region of uniaxial tension. However, they tend to underestimate the stresses under multiaxial loading since the interchain entanglements are ignored. Similar to the physical picture in [19,75], we consider a tube-like long polymer segment immersed in neighboring polymer chains. An element of it with a cross-sectional area confined by the surrounding chains has an areal deformation penalty:

$$\psi_e = \alpha k_B T \left(\frac{l^2}{d_0^2}\right) \nu^{-1}, \tag{16}$$

where $l = \sqrt{n}b$ and d_0 denote the initial mean square end-to-end distance and initial diameter of the tube, respectively; ν denotes the contraction of the cross-sectional area of the tube; α is the number factor which depends on the shape of the cross-section of the tube. The microscopic area contraction of such an incompressible tube is proportional to the reciprocal of axial elongation ($\nu = \frac{1}{\lambda^{axial}}$). Now we assume the mean axial elongation of tubes in the polymer network can be estimated via the general q-power mean of macroscopic principal stretches:

$$\langle \nu^{-1}\rangle = \langle \lambda^{axial}\rangle \approx \left(\frac{I_q}{3}\right)^{\frac{1}{q}}, \quad \text{with} \quad I_q := \lambda_1^q + \lambda_2^q + \lambda_3^q, \tag{17}$$

where q is a semi-empirically determined dimensionless material parameter that controls the softening behaviors of the polymer network. Note that I_q is a generalized invariant of the deformation gradient tensor $\boldsymbol{F}$ from the viewpoint of representation theory. For the case $q = 1$, $\langle \nu^{-1}\rangle$ equals the arithmetic mean of principal stretches. For $q = 2$, the tube constraint term degenerates to neo-Hookean form. For $q \to 0$, $\langle \nu^{-1}\rangle$ converges to the geometric mean and, physically, the volumetric deformation term. With Eq. (17), the free energy density contributed by the tube-like constraints can be approximately calculated via

$$\mathcal{F}_e = N_e\langle \psi_e\rangle = N_e\psi_e\left(\langle \nu^{-1}\rangle\right). \tag{18}$$

where N_e represents the number of entangled tubes per unit volume. Note that, although no approximation is essential in Eq. (18) since ψ_e is a linear function of the reciprocal of area contraction ν^{-1}, there could exist an alternative approach (for instance, [47]) to map macroscopic deformation to the mean microscopic tube area contraction $\langle \nu^{-1}\rangle$ for a better matching with the molecular measurements but adding parameters. The q-power mean we used just for it requires only one parameter to describe the non-ideal micro–macro mapping of tube deformation and works well within the present model. The role of q in phenomenological fitting will be discussed in Section 4.

3. Continuum constitutive model

So far, the microscopic effects taken into account in the present work have been described and connected to the macroscopic deformation gradient $\boldsymbol{F}$. In this section, we introduce a simple rational approximation of the inverse Langevin function and give closed-form macroscopic strain energy density functions against deformation. With these functions, we derive the engineering stresses under the incompressible constraint.

To simplify the macroscopic stretching free energy in Eq. (15), we introduce a reasonable approximation of the inverse Langevin function proposed by [76]

$$\mathcal{L}^{-1}(\mathrm{y}) \approx \frac{3\mathrm{y}}{\left(1-\mathrm{y}^2\right)\left(1+\frac{1}{2}\mathrm{y}^2\right)},$$
$$g(\mathrm{y}) := \mathrm{y}\mathcal{L}^{-1}(\mathrm{y}) - \ln\left(\frac{\sinh\left(\mathcal{L}^{-1}(\mathrm{y})\right)}{\mathcal{L}^{-1}(\mathrm{y})}\right) \approx \ln\left[\frac{1+\frac{1}{2}\mathrm{y}^2}{1-\mathrm{y}^2}\right], \tag{19}$$

where $\mathrm{y} \in [0,1)$ denotes a scalar variable. Although the approximation can be in other forms, Kröger approximation (Eq. (19)) was chosen for it exhibits correct asymptotic behaviors and improves the quality of the finite extendability potential of FJC without extra computational cost. It is important to distinguish between rational approximations of the inverse Langevin function, such as the Kröger approximation, and the RMS approximation criticized in Section 2. The former is a purely functional approximation that preserves the exact statistical–mechanical relation between force and chain extension, whereas the latter constitutes a mean-field closure at the ensemble level by replacing the average $\langle \bar{r} \rangle$ with the square root of the mean squared end-to-end distance $\sqrt{\langle \boldsymbol{r} \cdot \boldsymbol{r} \rangle}$. Consequently, the RMS approximation alters the micro–macro mapping prior to constitutive modeling, while the Kröger approximation used here acts only at the level of analytic representation.

Substituting Eqs. (8), (9) into Eq. (15) and taking the approximation Eq. (19), the free energy stored in the deformed polymer network is

$$\mathcal{F}_s = \mathcal{F}_{s,0} + Nk_BT\left[n\ln\left(\frac{1+\frac{\langle u\rangle}{2}}{1-\langle u\rangle}\right) - \ln\left(\frac{\sqrt{\langle u\rangle}}{(1-\langle u\rangle)\left(1+\frac{\langle u\rangle}{2}\right)}\right)\right], \tag{20}$$

where $\mathcal{F}_{s,0}$ is a constant free energy in reference state. In an isotropic polymer network, $\langle u\rangle$ can be evaluated by substituting Eqs. (13) and (14) into Eq. (12), the stretch free energy can be written as a function of the invariant:

$$\mathcal{F}_s = \mathcal{F}_{s,0} + Nk_BT\left[n\ln\left(\frac{3n+\frac{I_1}{2}}{3n-I_1}\right) - \ln\left(\frac{\sqrt{I_1}}{\left(3n-I_1\right)\left(6n+I_1\right)}\right)\right], \tag{21}$$

where $I_1 = \mathrm{tr}\,(\boldsymbol{B})$ is the first invariant of left Cauchy Green deformation tensor $\boldsymbol{B} = \boldsymbol{F}\cdot\boldsymbol{F}^T$. The first term in the square bracket consists of the classical stretch free energy in the eight-chain model. The second term emerges from the modification to the FJC free energy discussed in Section 2. Subject the free energy density to a linear elastomer limit, where the chain length is very large ($n \to \infty$), Eq. (21) converges to a Gaussian-statistical neo-Hookean free energy density augmented by a logarithmic hardening term:

$$\lim_{n\to\infty} \mathcal{F}_s(\boldsymbol{F}; n) = \frac{Nk_BT}{2}\left[\left(I_1-3\right) - \ln\left(\frac{I_1}{3}\right)\right]. \tag{22}$$

Interestingly, the functional form of Eq. (22) is asymptotically analogous, though not identical, to the reduced expression of the Anssari-Benam–Horgan model [58],

$$\mathcal{F} = \frac{3n(m-1)(1-n)}{2(1-mn)}G_s\left[\frac{1}{3n(m-1)}\left(I_1-3\right) - \ln\left(\frac{I_1-3n}{3-3n}\right)\right], \tag{23}$$

where structural restrictions on parameters n, m are relaxed to make them phenomenological real-valued parameters. Under the distinguished scaling $m = 1+\frac{1}{3n}$, the Anssari-Benam–Horgan free energy function exhibits, in the limit $n \to 0$, the same leading-order dependence on I_1 as Eq. (22), while differing by a constant prefactor. Accordingly, Eq. (22) may be regarded as an asymptotic reduction along a distinguished parameter path within the phenomenological family proposed by Anssari-Benam from a mathematical viewpoint [61].

The macroscopic free energy caused by interchain entanglements can be calculated by Eq. (18). To enforce the incompressibility of the polymer network ($J = \det(\boldsymbol{F}) = 1$) in the constitutive framework, a volumetric constraint term is incorporated into the total strain energy density function below:

$$\mathcal{F} = \mathcal{F}_s + \mathcal{F}_e - p(J-1), \tag{24}$$

where p is the Lagrangian multiplier and physically represents the hydrostatic pressure of the polymer network.

The total first Piola–Kirchhoff stress can be obtained by the partial derivative of Eq. (24)

$$\boldsymbol{P} = \frac{\partial\mathcal{F}}{\partial\boldsymbol{F}} = \underbrace{\frac{\partial\mathcal{F}_s}{\partial I_1}\frac{\partial I_1}{\partial\boldsymbol{F}}}_{\boldsymbol{P}^s} + \underbrace{\frac{\partial\mathcal{F}_e}{\partial\boldsymbol{F}}}_{\boldsymbol{P}^e} - pJ\boldsymbol{F}^{-T}, \tag{25}$$

where the relation $\partial J/\partial\boldsymbol{F} = J\boldsymbol{F}^{-T}$ has been used; $\boldsymbol{P}^s$ and $\boldsymbol{P}^e$ are the first Piola–Kirchhoff stress contributed by micro-stretch of FJC network and interchain entanglement, respectively. In the next section, Eq. (25) will be checked with classical hyperelastic material datasets. For practical purposes, we now derive the explicit expressions of $\boldsymbol{P}^s$ and $\boldsymbol{P}^e$. Invoking the relation $\partial I_1/\partial\boldsymbol{F} = 2\boldsymbol{F}$, $\boldsymbol{P}^s$ is calculated by

$$\boldsymbol{P}^s = G_s\left(\frac{n-1}{3n-I_1} + \frac{n+1}{6n+I_1} - \frac{1}{2I_1}\right)\boldsymbol{F}, \tag{26}$$

where $G_s = 2Nk_BT$ is the lumped macroscopic material parameter contributed by the stretch of the FJC network. The contribution of non-affine interchain entanglement to stress can be written in

$$\boldsymbol{P}^e = G_e\sum_{\alpha}^{3}\frac{\lambda_\alpha^{q-2}I_q^{\frac{1}{q}-1}}{3^{\frac{1}{q}}}\boldsymbol{F}\cdot\left(\boldsymbol{v}_\alpha\otimes\boldsymbol{v}_\alpha\right), \tag{27}$$

where $G_e = \alpha N_e k_B T\left(\frac{l^2}{d_0^2}\right)$ is the material parameter describing lumped strength of tube-like interchain effects; $\boldsymbol{v}_\alpha$ denotes the α-th eigen vector of $\boldsymbol{C}$ corresponding to the principal stretch λ_α. Appendix B provides the detailed derivation and frame-indifference check for Eq. (27). The invariant-dependent scalar prefactors in Eq. (26) and (27) are the mathematical source of strain-introduced anisotropy in isotropic hyperelastic materials studied recently in [77,78]. Since we have assumed a microscopic equilibrium state (Boltzmann equation used in Section 2), the system strain energy depends only on the macroscopic strain measures. Therefore, the second law of thermodynamics is trivially satisfied by zero dissipation:

$$\mathcal{D} = \boldsymbol{P} : \dot{\boldsymbol{F}} - \dot{\mathcal{F}} = 0. \tag{28}$$

In practice, the mechanical properties of hyperelastic polymer networks are usually measured in a plane stress state. Now we apply the present constitutive model to the general plane stress scenario ($\lambda_3 = (\lambda_1\lambda_2)^{-1}$, $P_3 = 0$) and give the explicit expression of stress for the model validation in the next section.

$$P_{1,2} = G_s\left(\frac{n-1}{3n-I_1} + \frac{n+1}{6n+I_1} - \frac{1}{2I_1}\right)\lambda_{1,2} + 3^{-\frac{1}{q}}G_eI_q^{\frac{1}{q}-1}\lambda_{1,2}{}^{q-1} - p\frac{1}{\lambda_{1,2}}, \tag{29}$$

with the hydrostatic pressure p calculated from $P_3 = 0$

$$p = G_s\left(\frac{n-1}{3n-I_1} + \frac{n+1}{6n+I_1} - \frac{1}{2I_1}\right)\left(\frac{1}{\lambda_1\lambda_2}\right)^2 + 3^{-\frac{1}{q}}G_eI_q^{\frac{1}{q}-1}\left(\lambda_1\lambda_2\right)^{-q}. \tag{30}$$

4. Model validation and discussion

In this section, we firstly use Eqs. (29), (30) to fit various stress–strain datasets of hyperelastic polymer networks, including vulcanized rubber [79,80], S4035A TPE [7], and Tetra-PEG gel [81]. Afterward, we compare the performance of the current model on Kawabata's dataset of isoprene rubber vulcanizate [82] to the other two existing

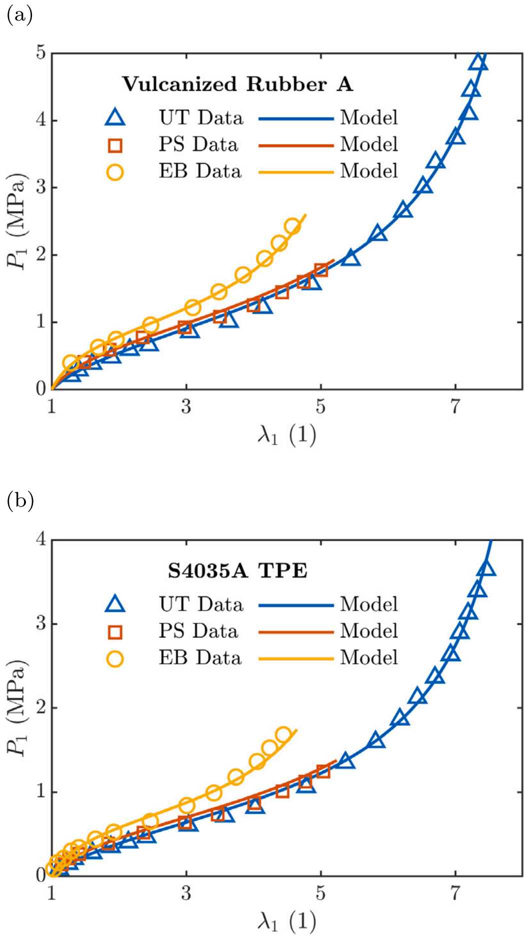

Fig. 4. Fitting results for two different hyperelastic materials. The scatter markers represent the experimental data, and the curves are obtained by the current model. (a) vulcanized rubber [79] and (b) S4035A TPE [7].

physics-based hyperelastic models proposed by Dal, et al. [69], Kaliske and Heinrich [43], together with a state-of-the-art invariant theory-based comprehensive model proposed by Anssari-Benam [61]. In the end, we conduct a parametric study on the current model and discuss the roles of parameters.

4.1. Fitting experimental data

We used the nonlinear least-squares curve fitting solver of MATLAB to extract the four parameters from the experimental data. Fig. 4 shows the stress–strain curves under basic plane loading modes, i.e., uniaxial tension (UT), pure shear (PS), and equibiaxial (EB) stretch. The results show that the current model is capable of accurately capturing the S-shaped softening–hardening tendency of the hyperelastic stress–strain curves in the full deformation regions. These two materials have similar Kuhn segment numbers in FJC ($n \approx 25$) and thus behave in similar stress–strain shapes in uniaxial loading modes (uniaxial tension and pure shear). For the test on the polymer networks with a higher crosslink density, the hardening stage emerges in an earlier deformation region, and the polymer networks with a lower crosslink density behave in contrast. To validate the correctness of the current model for those materials, data of another rubber vulcanized in a different condition (namely, vulcanized rubber B) [80] and two Tetra-PEG gels [81] were fitted. Fig. 5 shows the Cauchy stresses as a function of λ_1(or λ_3) with constrained λ_2 of $1, 1.502, 1.984, 2.295$ and 2.2623, respectively. The black and colored dashed lines mark the contour of the uniaxial tension and theoretical extension limits with different constant λ_2, respectively. This way of organizing data follows the original figure in [80]. Fig. 6 shows the fitting results for Tetra-PEG gels prepared with two different recipes [81] under equibiaxial (EB), pure shear (PS), and unequal biaxial (UB) stretching. For the unequal biaxial stretching case, the deformation ratio was fixed to $\lambda_2 = \left(\lambda_1 + 1\right)/2$. The model predictions show good agreement with the experimental data of general plane stress modes and demonstrate that the current model is transferable among different hyperelastic materials with various segment numbers n. The material parameters used in Figs. 4, 5, and 6 are listed in Table 1. Note that for real polymer networks, the average segment number n over all FJCs may not be an integer due to fluctuation in chain configuration. However, to keep the consistency with the physics interpretation in Section 2, the fitted n are forced to be integers via a two-step procedure consisting of an initial continuous fit to estimate n, followed by refitting with n constrained to integer values neighboring the initial estimation.

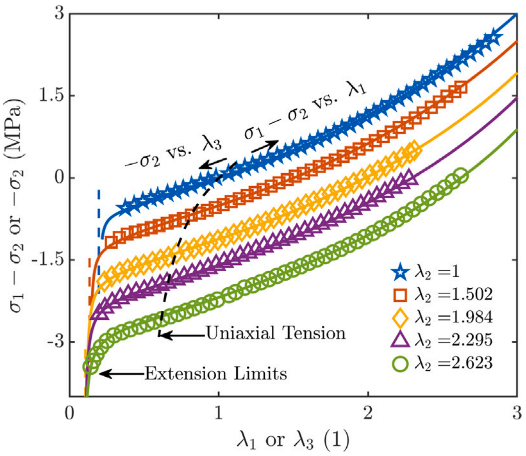

Fig. 5. Biaxial Cauchy stress of vulcanized rubber B [80] against different fixed λ_2. Colored solid lines are the prediction of the current model with fitted parameters. The black dashed line indicates the contour of uniaxial tension, which separates the two kinds of curves. left side $-\sigma_2$ against λ_3 and right side $\sigma_1-\sigma_2$ against λ_1. Colored dashed lines present the theoretically predicted extension limits.

4.2. Comparison with existing models

Following the review of [23], the general biaxial stretching dataset of isoprene rubber vulcanizate measured by [82] is used to validate the current model. In that review, authors compared representative existing models developed in the recent decades, and only a few reach a good trade-off between complexity and accuracy in fitting that dataset. Two highly ranked physics-based models, the Langevin chain-based extended eight-chain model [69] and the four-parameter extended tube model [43], are chosen to be compared with the present constitutive model. In addition, a recently proposed four-parameter “comprehensive” model [61], which combines the Langevin chain physics and representations generalization, is also compared due to its I_q-dependency.

The extended eight-chain model has the total deformation energy density function as follows:

$$\mathcal{F} = G_s n \ln\left(\frac{3n - \frac{1}{2}I_1}{3n - I_1}\right) + G_e \sqrt[3]{\frac{I_2}{3}}, \tag{31}$$

where $I_2 = \lambda_1^2\lambda_2^2 + \lambda_1^2\lambda_3^2 + \lambda_2^2\lambda_3^2$ is the second invariant of right Cauchy–Green deformation tensor; The inverse Langevin function in original [69] is approximated via Eq. (19) for computational convenience.

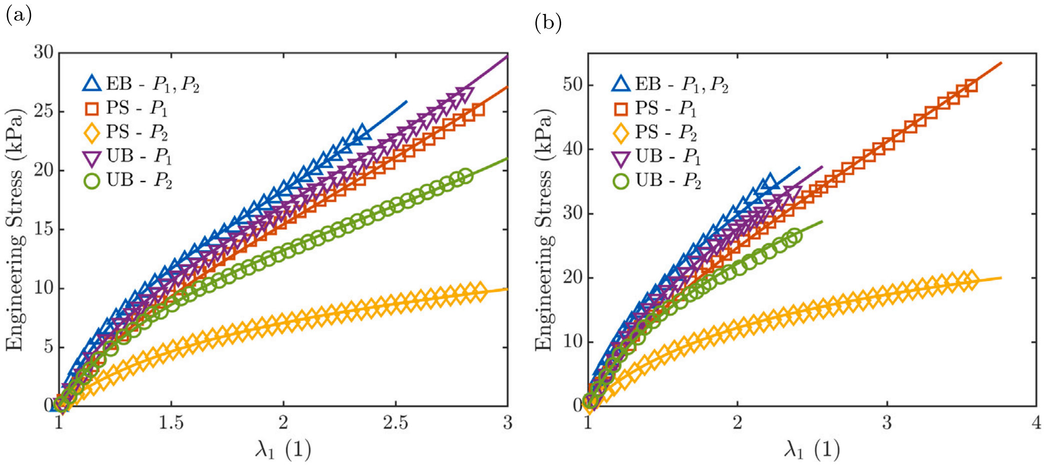

Fig. 6. Fitting results of two gels [81]: (a) Tetra-PEG A (n = 14); (b) Tetra-PEG B (n = 45), under equibiaxial (EB), pure shear (PS), and unequal biaxial (UB, $\lambda_2 = (\lambda_1 + 1)/2$) loadings. The scatter markers represent the experimental data, and the solid curves are stress predicted by the current model.

Table 1
Fitted material parameters for various hyperelastic polymer networks.

Polymer	n (1)	G_s (MPa)	G_e (MPa)	q (1)	E_e/E_s (1)
Vulcanized rubber A	26	0.2617	4.389	0.2035	0.8453
S4035A TPE	25	0.1773	3.1275	0.2328	1.0167
Vulcanized rubber B	9	0.1810	2.011	0.9910	2.6820
Tetra-PEG gel A	14	7.542×10^{-3}	13.54×10^{-3}	1	0.4412
Tetra-PEG gel B	45	12.94×10^{-3}	60.29×10^{-3}	0.3299	0.3822

Table 2
Fitted material parameters for isoprene rubber vulcanizate in the compared models [82].

Model	n or δ^2 (1)	G_s (MPa)	G_e (MPa) or m (1)	q (1)
Current model	13	0.1304	1.9244	0.9375
Extended eight-chain	200	0.2829	0.3938	–
Extended tube	0.0108	0.1666	0.23539	−0.6220
Four-parameter comprehensive	8.375	0.7850	25	1.3457

The extended tube model has the following total deformation energy density function.

$$\mathcal{F} = \frac{1}{2}G_s\left[\frac{(1-\delta^2)(I_1-3)}{1-\delta^2(I_1-3)} + \ln\left(1-\delta^2(I_1-3)\right)\right] + \frac{2G_e}{q^2}\sum_{\alpha=1}^{3}\left(\lambda_\alpha^{-q}-1\right), \tag{32}$$

where G_s and G_e are two constants related to microscopic effects; Dimensionless material parameters δ and p measure the finite extensibility of individual polymer chains and the contribution of interchain entanglements, respectively.

The four-parameter comprehensive model has the following total deformation energy density function:

$$\mathcal{F} = \frac{3n(m-1)}{2m}G_s\left[\frac{1}{3n(m-1)}\left(I_q-3\right) - \ln\left(\frac{I_q-3n}{3-3n}\right)\right], \tag{33}$$

where G_s, m are model parameters; n constraints the extension limit; The parameter q is implicitly included in generalized invariant I_q, which has the same definition as in (17).

The comparison between the predictions of four models for isoprene rubber vulcanizate is shown in Figs. 7, 8. Figs. 9 and 10 provide zoom-ins in low to moderate deformation regimes ($\lambda_1 \leq 1.3$) of fitted P_1, P_2, respectively. The colored solid lines are model predictions with the material parameters (see Table 2). The black dash-dot lines guide stress curves for the experimental data under three basic loading modes.

In addition, we use the average relative error (ARE) suggested by [83] to evaluate the quality of the fitting. Its definition is

$$ARE = \frac{1}{n_{data}}\sum_{\beta}^{n_{data}}\frac{\left|P_\beta^{theo}-P_\beta^{exp}\right|}{P_\beta^{exp}}, \tag{34}$$

where P^{exp} and P^{theo} are stress data and theoretically predicted values; Data points are numbered by β; n_{data} is the total number of data points to be averaged. Specifically, the P_2 data of uniaxial tensile loading mode were filtered out since their relative errors are ill-defined.

Total ARE and ARE under three basic deformation modes corresponding to four models are listed in Table 3. Fig. 11 gives a detailed comparison of the ARE of models for different constrained λ_1. Unsurprisingly, three four-parameter models approximately half the ARE in the complicated biaxial loading scenario compared to the extended eight-chain model, since they have one more parameter to capture the non-ideal micro–macro transition or interchain effects. Compared to the extended tube model, the current model has a lower ARE at both low and high stretch levels, while exhibiting a slightly higher ARE at moderate stretch levels. In contrast, the four-parameter comprehensive model (23) exhibits a slightly better performance at a wide moderate stretch regime, while it has an abnormally high ARE at a small stretch level. The same phenomenon was also observed in other materials as presented in the original literature [61]. Such a drawback of the four-parameter comprehensive model shall be attributed to its functional form, which directly substitutes the average non-affine chain

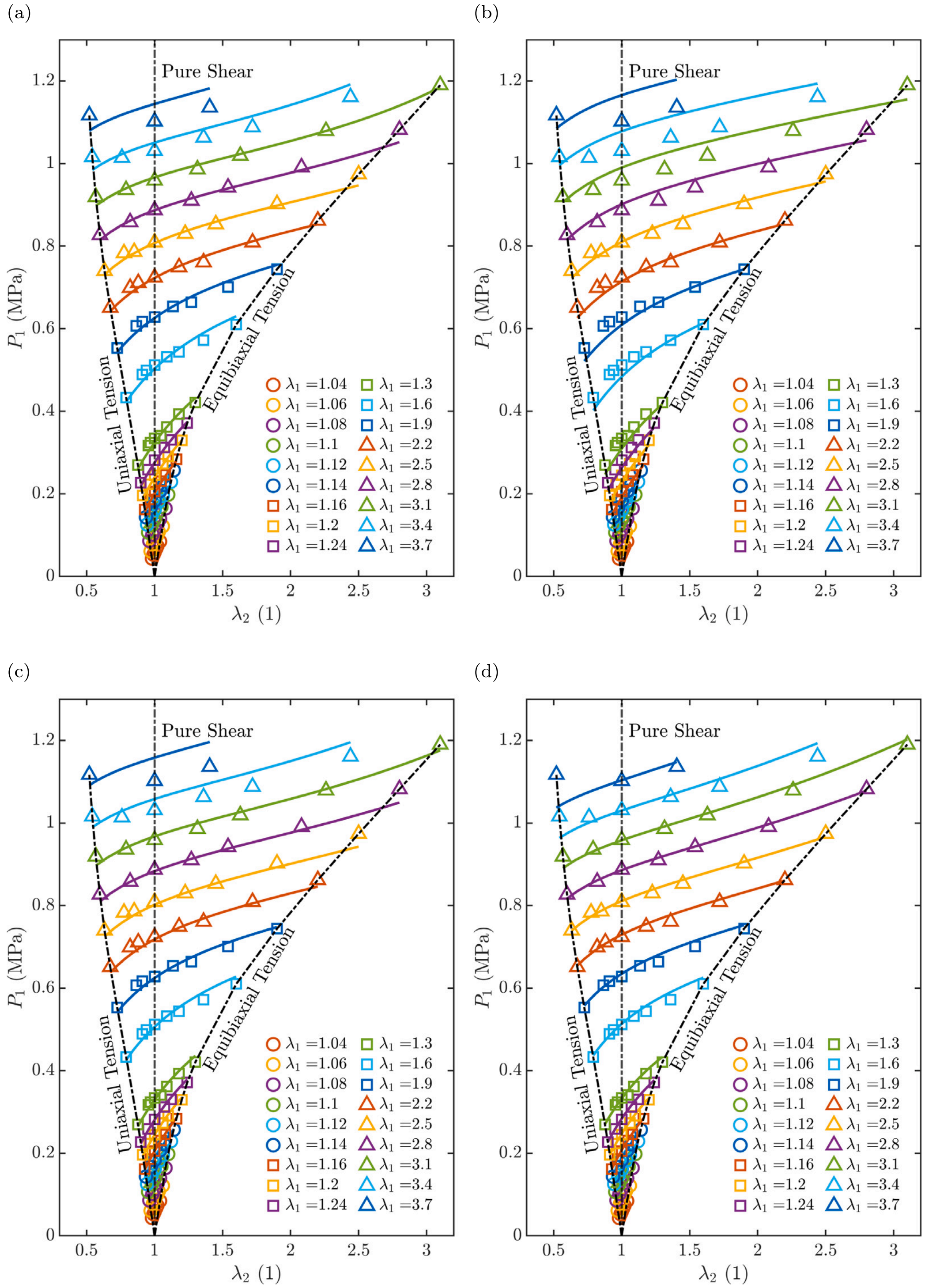

Fig. 7. P_1 predicted by models for isoprene rubber vulcanizate under different pre-strain λ_1 from Kawabata dataset [82]. (a) The current model; (b) Extended eight-chain model; (c) Extended tube model; (d) Four-parameter comprehensive model.

stretch (on macroscopic I_q) into the Padé approximation to the inverse Langevin function. That implicitly forbids an energy contribution from interchain entanglements, which shall follow a different microscopic entropic function rather than the inverse Langevin form. Even though some tube models, for instance, [71], can be specialized to a special composite formulation of three instances of functional form (33) as demonstrated in [61], those instances are associated separately with different microscopic mechanisms, i.e., chain stretch and tube confinement. Therefore, this study is apt to compose the chain stretch and interchain effects, each of which may have a different functional representation, additively, rather than generalizing any single functional representation with an increasing number of parameters, even though that approach, as suggested in [61,64], is mathematically general.

Worth mentioning that the three-parameter inverse Langevin chain-based models like [44,69] may sacrifice the physical meaning of n to compensate for the contribution of non-ideal micro–macro transition of large multi-axial loading modes, which is usually described by the power term q in the four-parameter tube-like models. The isoprene rubber vulcanizate measured by [82] shall have a similar chain network as

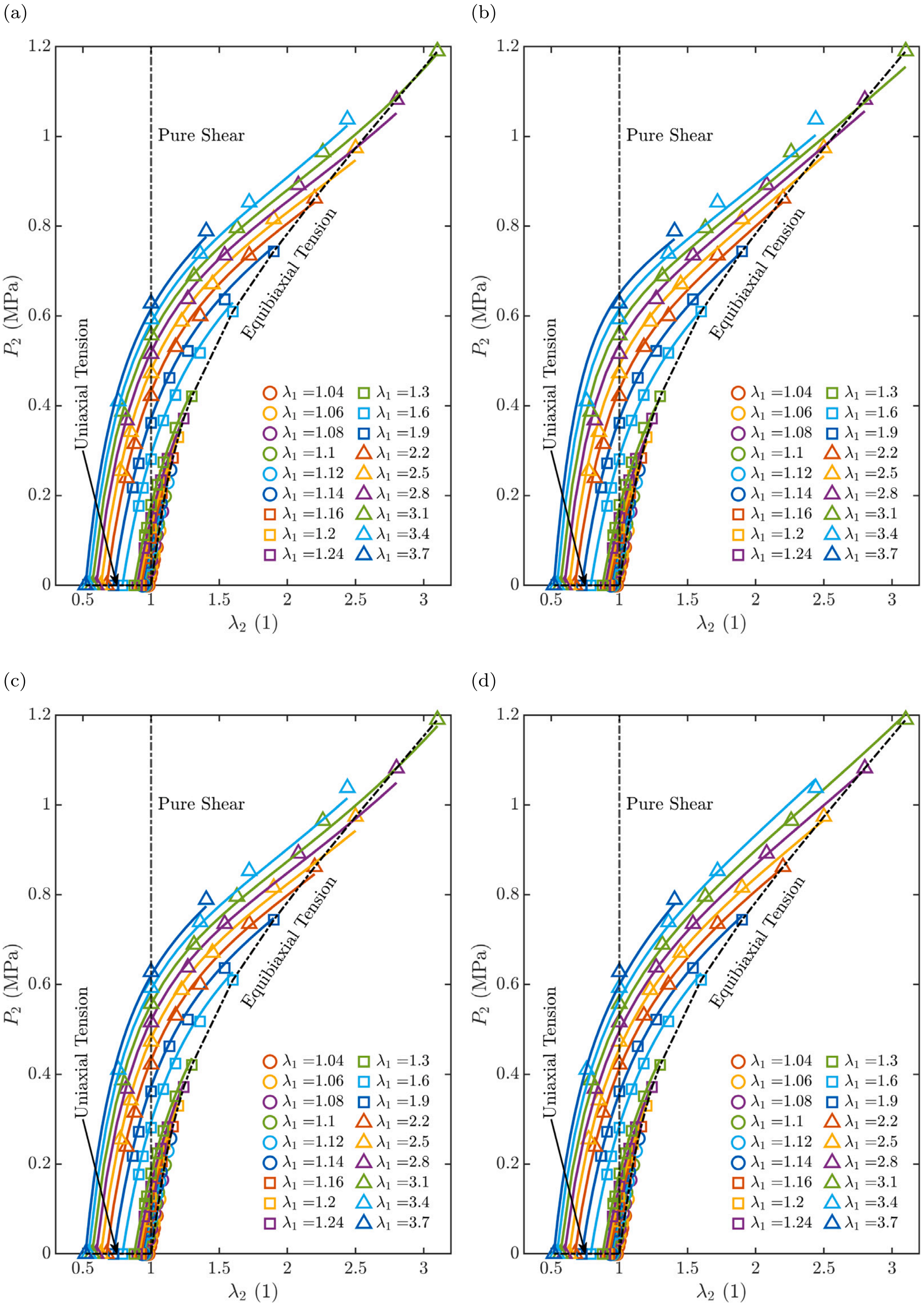

Fig. 8. P_2 predicted by models for isoprene rubber vulcanizate under different pre-strain λ_1 from Kawabata dataset [82]. (a) The current model; (b) Extended eight-chain model; (c) Extended tube model; (d) Four-parameter comprehensive model.

vulcanized natural rubbers, and is unlikely to reach an extremely lightly crosslinked network structure with $n > 100$ in physics. In fact, we also notice the abnormally high n during fitting other widely used general three-parameter elastomer models, for instance, the general elastomer model proposed by [44] has the number of Kuhn segments n reaching around 500 for the Kawabata dataset, but still with considerable ARE. It is clear that those large n are physically meaningless for the vulcanized rubber networks. Therefore, we underscore that the physically based models shall include at least four parameters to properly cover the deformation-induced softening of tube-like constraints. The current model has a comparable accuracy to the extended tube model among four-parameter models. Meanwhile, the extended tube model needs to change the sign of q from material to material for phenomenological accuracy, which is considered physically meaningless [43]. Besides, if the power parameter q in the extended tube model is strictly constrained to a non-negative region to keep the physical meaning during fitting, one may find $q \to 0$ for some materials like the Kawabata dataset to get the best fitting. For these materials, the entangled term reduces to Hencky

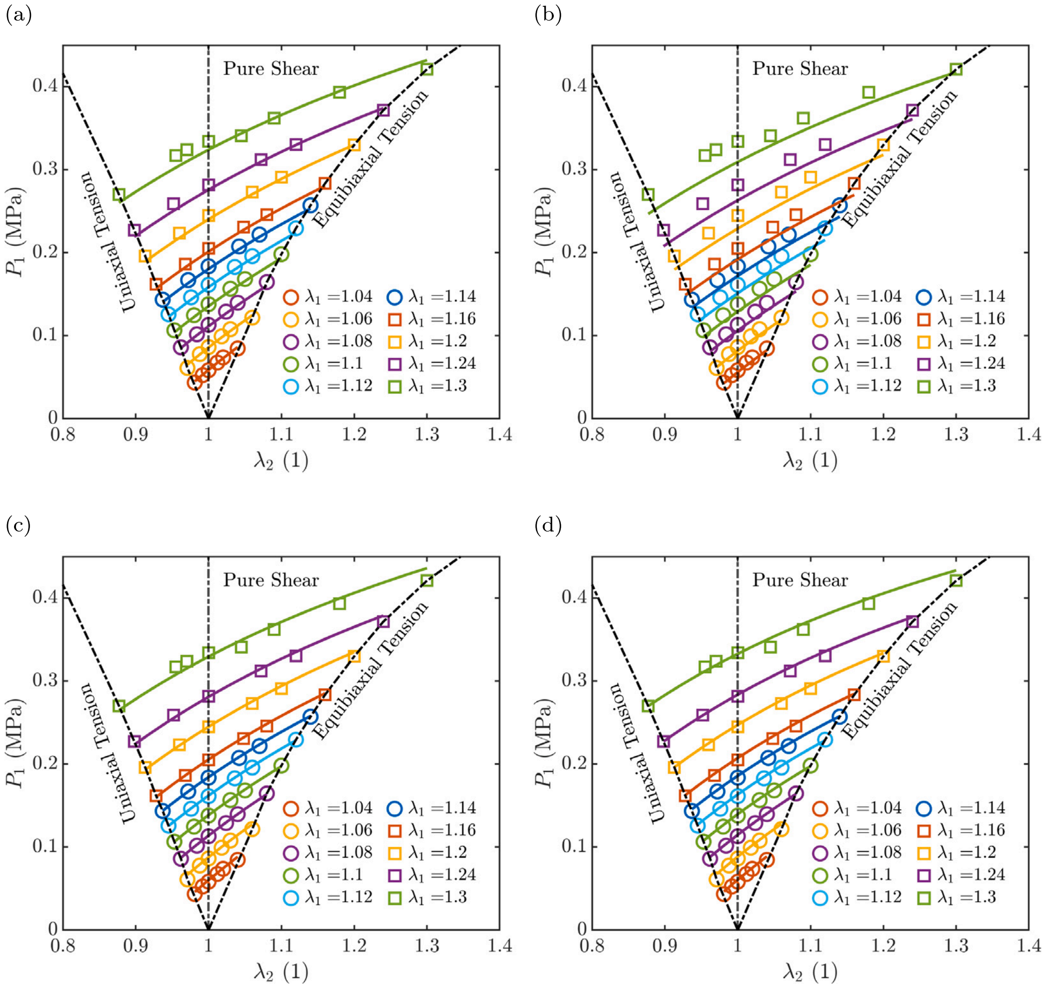

Fig. 9. Zoom-in of P_1 within the low to moderate deformation regimes ($\lambda_1 \leq 1.3$) corresponding to Fig. 7 . (a) The current model; (b) Extended eight-chain model; (c) Extended tube model; (d) Four-parameter comprehensive model.

Table 3
ARE (%) of models from Kawabata dataset [82].

Model	UT	PS	EB	Total
Current model	2.986	1.864	1.868	1.943
Extended eight-chain	6.376	3.511	4.028	3.781
Extended tube	2.210	1.811	2.341	2.143
Four-parameter comprehensive	2.174	1.727	2.308	1.928

logarithmic strain energy form [84] via asymptotic analysis at the limit $q \rightarrow 0$. Although the four-parameter comprehensive model achieves a smaller value of n compared to the current model, it predicts higher theoretical uniaxial and equibiaxial stretch limits, $\lambda_{UT}^{limit} = 10.85$ and $\lambda_{EB}^{limit} = 6.56$, compared to those, $\lambda_{UT}^{limit} = 6.22$ and $\lambda_{EB}^{limit} = 4.42$, predicted by current model for (33) constrains the generalized invariant I_q instead of I_1. Chain extendabilities predicted by both current model and four-parameter comprehensive model are within a reasonable range in chemistry. However, m and q in the model (33) are both semi-empirically defined. Moreover, the connection between parameter n of (33) and the microscopic physical picture has been broken.

As a closing remark of the comparative study, the current model preserves the physical interpretation of material parameters and maintains the form of the free energy function, while achieving competitive phenomenological accuracy for the material data studied above.

4.3. Discussion on parameters

It can be intuitively seen that two constants G_e and G_s control only the magnitude of the chain stretch stress and entangled stress, and the dimensionless parameters n and q control the shape of the stress–strain curve. A parametric study is conducted to discuss the impact of dimensionless parameters n and q on the shape of the predicted stress–strain curve. We now consider the normalized free energy contributed by the stretch of FJC network. The comparison on normalized $\mathcal{F}^s$ against I_1 prediction between the prediction of the current model and the classical eight-chain model is shown in Fig. 12. The Kuhn segment number n controls the theoretical macroscopic stretching limit as it does in the eight-chain model. However, the current model tends to predict a softer response of the FJC network in the low and moderate stretch levels, followed by a sharper increase in stress when the response approaches the non-Gaussian regime for a high stretch level. Compared to the eight-chain model, such a tendency generally leads to a higher fitted value of G_s and a lower fitted value of n on the same material. In consequence, the current model requires a higher percentage of contribution from the interchain entanglement at the low stretch level. The case study on the uniaxial tension data of vulcanized rubber A is shown in Fig. 13. The black solid lines give the prediction of the current model shown in Fig. 4(a) with parameters listed in Table 1, and dashed lines give the share of contributions from chain stretch and interchain entanglement. In this case, the chain stretch and interchain entanglement both have

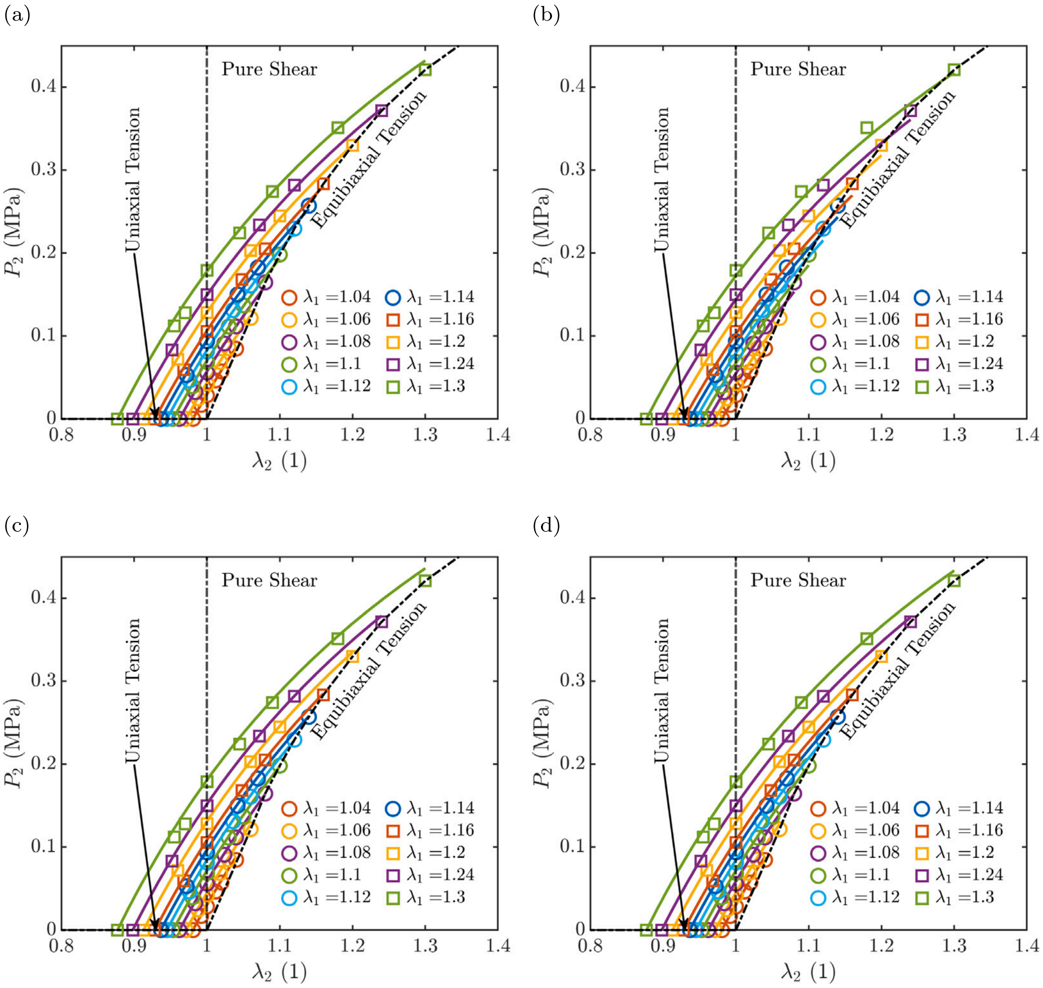

Fig. 10. Zoom-in of P_2 within the low to moderate deformation regimes ($\lambda_1 \le 1.3$) corresponding to Fig. 8 . (a) The current model; (b) Extended eight-chain model; (c) Extended tube model; (d) Four-parameter comprehensive model.

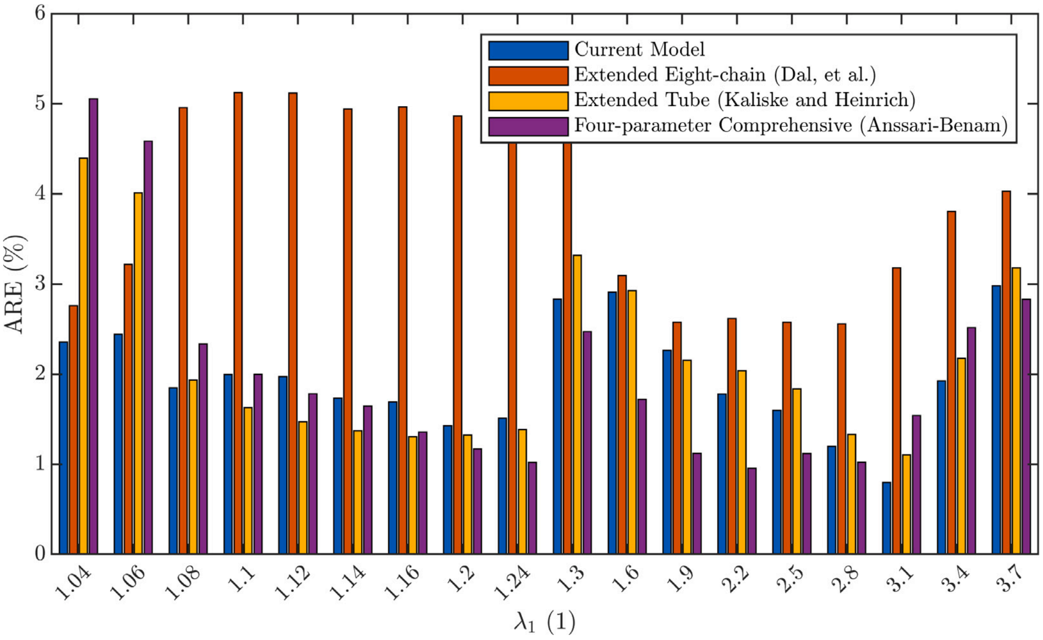

Fig. 11. ARE of different constitutive models evaluated at various stretches λ_1, using the Kawabata dataset [82].

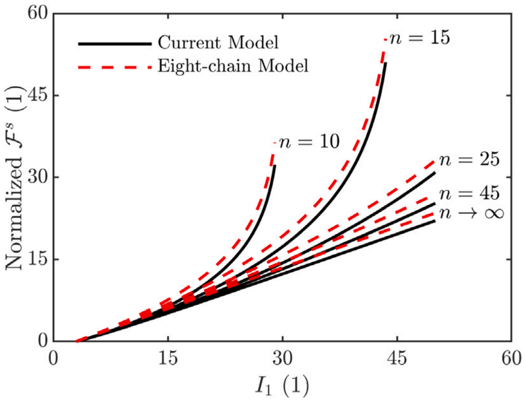

Fig. 12. Comparison on the normalized free energy of stretch FJC network between the current model and classical eight-chain model.

considerable impacts on the stiffness at the early tensile stage ($\lambda_1 < 1.5$ for vulcanized rubber A). The entangled stress reaches a "saturated" state at a moderate stretch level and dominates the softening behavior while the chain stretch contribution is still in the Gaussian region. In the tail of the S-shape stress–strain curve, the chains in the polymer network reach the non-Gaussian stage; hence, the stretch contribution dominates the stiffening. ∞

The uniaxial isochoric deformation $\boldsymbol{F} = \lambda \boldsymbol{v}_1 \otimes \boldsymbol{v}_1 + \frac{1}{\sqrt{\lambda}} \boldsymbol{v}_2 \otimes \boldsymbol{v}_2 + \frac{1}{\sqrt{\lambda}} \boldsymbol{v}_3 \otimes \boldsymbol{v}_3$ provides a path to evaluate the Young's modulus in infinitesimal deformation limit, which is a reasonable stress normalization factors for parametric study. The moduli originate from the chain stretch, and the interchain entanglement can be evaluated via

$$E_s = \left.\frac{\partial^2 \mathcal{F}_s}{\partial \lambda^2}\right|_{\lambda=1} = \frac{4n+3}{2n+1} G_s, \quad E_e = \left.\frac{\partial^2 \mathcal{F}_e}{\partial \lambda^2}\right|_{\lambda=1} = \frac{q}{2} G_e. \tag{35}$$

The ratios of stretched and entangled Young's moduli for different polymer networks are listed in Table 1. Consider a normalized entangled stress $\bar{P}^e_1 = P^e_1 / E_e$, the stress–strain curves under uniaxial tension and equibiaxial stretch with different q are shown in Fig. 14. The results show that q is the control parameter for the divergence between uniaxial tension and equibiaxial stretch stress–strain curves. A large $q \to 1$ leads to a similar saturated stress under uniaxial tension and equibiaxial stretch. The divergence in $\bar{P}^e_1$ increases with the decrease of q. In addition, for very small $q = 0.2$ (e.g., vulcanized rubber A and TPE discussed above), a significant softening appears after the stretch level reaches the saturated $\bar{P}^e_1$.

4.4. Limitation and outlook

Although the current model only discusses isotropic hyperelastic behavior and is validated by monotonic loading data, the idea of constructing a free energy density function of the squared end-to-end distance can be readily adopted by adding internal variables to capture more complex phenomena, for example, Mullins effect, hysteresis of cyclic, viscosity, creeping, etc. By introducing an anisotropic network metric to Eq. (11), one can derive a non-Gaussian elasticity to an anisotropic polymer network like liquid crystal elastomers or other rubber-like bio materials [74]. The curing [85] and damage [86] effects can also be introduced to the current framework by considering active chain length $n(t)b$ and chain density $N(t)$ depending on chemical kinetics. The mean field approximation Eq. (15) kept in the current model is still not mathematically strict, thus may be further improved via introducing a sharpened Jensen's inequality [87–89] to better describe the non-linear behavior at high stretch level. The statistical accuracy of the averaging (15) may be further evaluated by a FEM simulation of network mechanics as suggested by [90,91]. Meanwhile, such improvements will obviously either increase the mathematical complexity or be subject to numerical feasibility constraints. Some alternative chain statistics based on alternative microscopic physics assumptions, for instance, Rayleigh exact non-Gaussian distribution [92] or non-rigid bond [93,94], can potentially be introduced to modify the form of the single-chain free energy density function. By adding instances in the functional form of Eq. (18) with more parameters $\{q_1, q_2, \ldots\}$, the capability of the current model in tracking the interchain effects and multiaxial behaviors may be further improved in the sense of [47]. Addressing these aspects constitutes a natural extension of the present framework and will be pursued in future work.

5. Conclusions

This article proposed a new physics-motivated four-parameter constitutive relation of the hyperelastic polymer networks. The model combines a modified single-chain finite extendability and a non-affine interchain entanglement contribution. Starting from the issue of the RMS approximation, which is widely employed in classical polymer network models such as the Arruda–Boyce eight-chain model [13] and its successors [44,69], we derived a single-chain free energy expressed as a function of the squared end-to-end distance, thereby avoiding the need for the RMS approximation in micro-to-macro free energy mapping. Assuming a Boltzmann distribution of end-to-end distance, the derived freely jointed chain free energy was checked via a Monte Carlo sampling simulation. The implicit inverse Langevin function in the free energy expression is substituted by an elementary function via Kröger's approximation [76] to reach a good trade-off between complexity and accuracy. In addition, we introduced a correction term that microscopically originates from the tube-like interchain effects [39,43,75] into the total hyperelastic free energy. By assuming an ideally affine micro–macro deformation mapping of second moment of end-to-end vectors and a non-affine area contraction of microscopic tube confinements, the macroscopic deformation free energy is derived in the sense of mean field. An explicit macroscopic constitutive model of a hyperelastic polymer network and the expression of engineering stress components at the plane stress limit are obtained for the validation with experimental data.

The model was validated with experimental data from various polymer networks, including vulcanized natural rubber, S4035A TPE, Tetra-PEG gel, and isoprene rubber vulcanizate. The loading conditions of experimental data contain three simple plane stress modes as well as more general biaxial stretch. We demonstrate that our model can accurately capture the mechanical behaviors of hyperelastic polymer networks with either short or long chains, which quantitatively correspond to a span of Kuhn segment numbers n varying from 9 to 45. The performance of the current model is compared with three other successful existing models, the eight-chain model [69], the extended tube model [43], and the four-parameter comprehensive model [61] on the general biaxial stretch dataset of isoprene rubber vulcanizate [82]. The comparison shows that the current model has a compatible phenomenological accuracy without sacrificing the physical interpretations of parameters or changing the mathematical form of the constitutive relation at the asymptotic limit of the fitted parameter. In a parametric study, we demonstrate how two dimensionless parameters n and q control the shape of the stress–strain curve. Compared to the end-to-end-distance-based model, the current squared-distance-based model has a stretching limit controlled by n but tends to predict a higher weight of entangled effect in total stress in the small deformation limit. The semi-empirical averaging parameter q controls the divergence between stress–strain curves of uniaxial tension and equibiaxial stretch. Compared to the comprehensive model, the current model explicitly distinguishes the contributions of FJC network stretch and tube confinement. Future work will extend the framework of the current

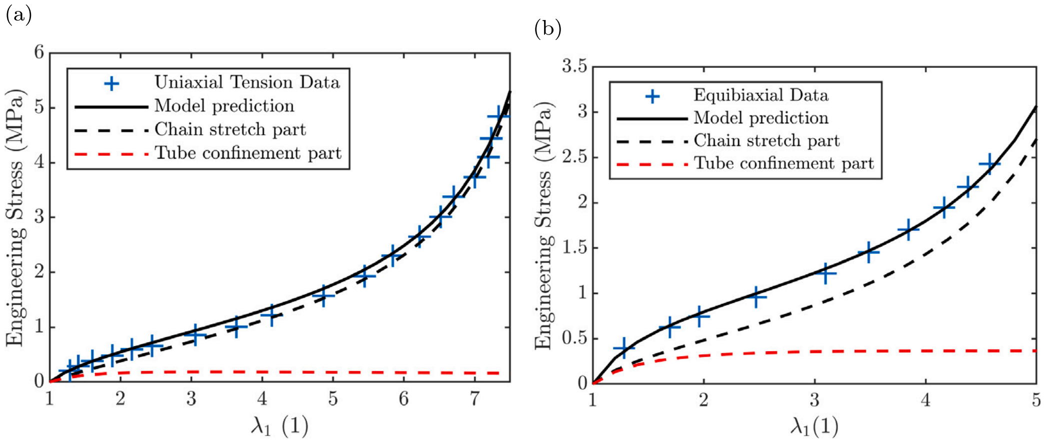

Fig. 13. The stress–strain curve of vulcanized rubber A with separated contributions from chain stretch and interchain entanglements at: (a) uniaxial tension condition; (b) equibiaxial stretch condition.

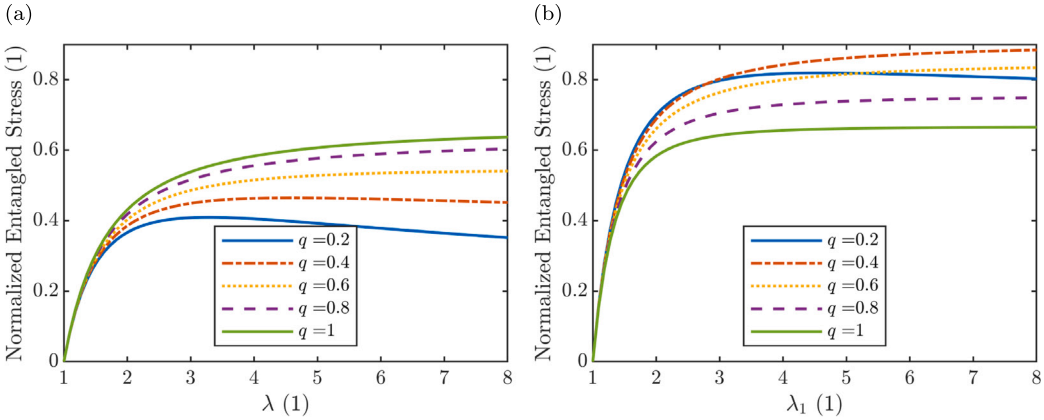

Fig. 14. Normalized entangled stress $\bar{P}_1^e$ with different values of q under (a) uniaxial tension; (b) equibiaxial stretch.

study to more complicated non-ideal polymer networks with dissipative behaviors.

In summary, this study resolves a long-standing conceptual mismatch in the physical interpretation of eight-chain hyperelastic theory by reformulating the microscopic free energy of freely-jointed chains. When augmented with a generalized q-mean statistical description of tube-like interchain constraints, the proposed model achieves phenomenological accuracy in predicting the multiaxial mechanical response of polymer networks that is comparable to established tube-based and comprehensive models, while offering a clearer micro–macro physical interpretation. This provides a consistent and well-founded starting point for further development of constitutive theories for soft materials.

CRediT authorship contribution statement

Zichuan Li: Writing – original draft, Visualization, Validation, Project administration, Methodology, Investigation, Formal analysis, Data curation, Conceptualization. **Jiajie Fan:** Writing – review & editing, Supervision, Funding acquisition. **Guoqi Zhang:** Writing – review & editing, Supervision, Project administration, Funding acquisition.

Declaration of competing interest

The authors declare that they have no known competing financial interests or personal relationships that could have appeared to influence the work reported in this paper.

Acknowledgments

This work is supported by the European Union's Horizon 2020 research and innovation program under grant agreement No 952166 (REPAIR).

Appendix A. Monte Carlo sampling used in current study

Monte Carlo sampling is used in Section 2 to visualize the structural difference between RMS and mean value (Fig. 2), and to demonstrate the performance of the probability density function $p_u(u)$ (Fig. 3). In the current simulation, the total number of FJCs in the ensemble N_{MC} was set to 10^7 to obtain stable histogram probability density estimates with 100 counting bins. In practice, the large ensemble was divided into a loop over several chunks of size $N_{chunk} < N_{MC}$ for convenience in memory management, with the purpose of reproducibility and robustness of the home-made MATLAB script. In each chunk, $N_{chunk} \times n$ independent random unit vectors $\boldsymbol{u}_\alpha$ were generated via Gaussian normalization [95] and assembled into N_{chunk} FJCs with end-to-end vectors $\boldsymbol{r}_\beta$. Then derived quantities of interest (i.e., u, $\bar{r}$, r_z) are evaluated based on $\boldsymbol{r}_\beta$, and their contributions are accumulated into running histograms or statistical averages before discarding intermediate data of $\boldsymbol{u}_\alpha$, $\boldsymbol{r}_\beta$. On the test system, a single-chunk simulation at $N_{chunk} = 10^7$, $n = 30$ resulted in a peak memory usage of merely $<$ 15 GB; chunking is therefore not strictly required for feasibility at this size but is retained for the

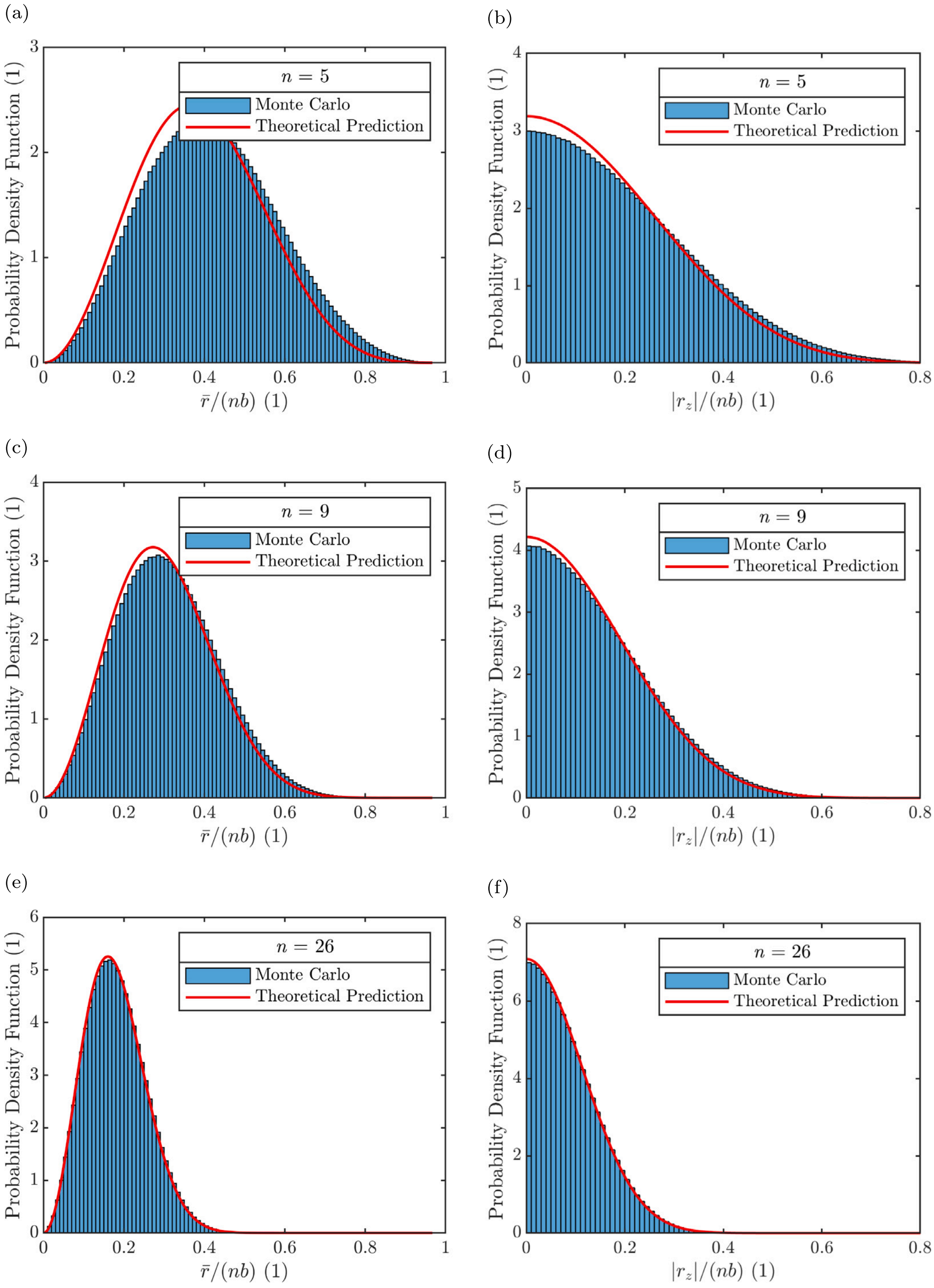

Fig. A.15. Comparison on the probability densities of normalized end-to-end distance $\bar{r}/(nb)$ (left) and $|r_z|/(nb)$ (right) predicted by theory and Monte Carlo sampling with the number of segments: (a)(b) $n = 5$; (c)(d) $n = 9$; (e)(f) $n = 26$.

simulation of larger ensembles or longer FJCs. The probability density functions p_z, $p_{\bar{r}}$ (Eq. (1),(4)) were also evaluated and shown in Fig. A.15.

Appendix B. Derivation and frame-indifference check of entangled stress

The evaluation of $\boldsymbol{P}^e$ needs the eigen equation $\boldsymbol{C} \cdot \boldsymbol{v}_\alpha = \lambda_\alpha^2 \boldsymbol{v}_\alpha$, which can be written in the scalar function of $\boldsymbol{F}$

$$\lambda_\alpha^2 = \left(\boldsymbol{F} \cdot \boldsymbol{v}_\alpha \otimes \boldsymbol{v}_\alpha \right) : \boldsymbol{F}, \tag{B.1}$$

Then the partial derivative of the principal stretch with respect to the deformation gradient $\boldsymbol{F}$ is

$$\frac{\partial \lambda_\alpha}{\partial \boldsymbol{F}} = \frac{1}{\lambda_\alpha} \left(\boldsymbol{F} \cdot \boldsymbol{v}_\alpha \otimes \boldsymbol{v}_\alpha \right), \tag{B.2}$$

and the slopes of entangled energy against principal stretches are obtained by the chain rule

$$\frac{\partial \mathcal{F}_e}{\partial \lambda_\alpha} = \frac{\partial \mathcal{F}_e}{\partial I_q} \frac{\partial I_q}{\partial \lambda_\alpha} = G_e \frac{\lambda_\alpha^{q-1} I_q^{\frac{1}{q}-1}}{3^{\frac{1}{q}}}, \tag{B.3}$$

Substituting (B.2) and (B.3) into the chain rule

$$\boldsymbol{P}_e := \frac{\partial \mathcal{F}_e}{\partial \boldsymbol{F}} = \frac{\partial \mathcal{F}_e}{\partial \lambda_\alpha} \frac{\partial \lambda_\alpha}{\partial \boldsymbol{F}}, \tag{B.4}$$

entangled stress (27) is obtained.

It is trivial to see that $\boldsymbol{P}^s$ and the incompressibility constraint term hold the principle of material frame-indifference, and we check the entangled stress $\boldsymbol{P}^e$ below. Given a new deformation gradient tensor $\boldsymbol{F}^* = \boldsymbol{o} \cdot \boldsymbol{F} \cdot \boldsymbol{O}^T$ under arbitrary rigid rotation $\boldsymbol{o} \in Orth^+$ and proper orthogonal transformation $\boldsymbol{O} \in Otho^+$, the new entangled stress $\boldsymbol{P}^{e*}$ is

$$\boldsymbol{P}^e\left(\boldsymbol{F}^*\right) = G_e \sum_{\alpha}^{3} \frac{\lambda_\alpha^{*\,q-2} I_q^{*\,\frac{1}{q}-1}}{3^{\frac{1}{q}}} \boldsymbol{F}^* \cdot \left(\boldsymbol{v}_\alpha^* \otimes \boldsymbol{v}_\alpha^*\right), \tag{B.5}$$

with $\boldsymbol{v}_\alpha^*$ the eigen vectors of new right Cauchy–Green deformation tensor $\boldsymbol{C}^*$. The values of principal stretches are unchanged for any $\boldsymbol{o}$ and $\boldsymbol{O}$, so are their symmetric scalar functions (i.e., $\lambda_\alpha^* = \lambda_\alpha$ and $I_q^* = I_q$). Besides, for symmetric right Cauchy–Green deformation tensor, $\boldsymbol{C}^* = \boldsymbol{O} \cdot \boldsymbol{C} \cdot \boldsymbol{O}^T$, the eigen vectors rotate by $\boldsymbol{v}_\alpha^* = \boldsymbol{O} \cdot \boldsymbol{v}_\alpha$. Then Eq. (B.5) satisfies the principle of material frame-indifference

$$\boldsymbol{P}^e(\boldsymbol{F}^*) = \boldsymbol{o} \cdot \boldsymbol{P}^e(\boldsymbol{F}) \cdot \boldsymbol{O}^T. \tag{B.6}$$

Data availability

Data will be made available on request.

References

[1] Han F, Li M, Ye H, Zhang G. Materials, electrical performance, mechanisms, applications, and manufacturing approaches for flexible strain sensors. Nanomaterials 2021;11(5):1220, URL: https://www.mdpi.com/2079-4991/11/5/1220.

[2] Ferrantini C, Pioner JM, Martella D, Coppini R, Piroddi N, Paoli P, Calamai M, Pavone FS, Wiersma DS, Tesi C, Cerbai E, Poggesi C, Sacconi L, Parmeggiani C. Development of light-responsive liquid crystalline elastomers to assist cardiac contraction. Circ Res 2019;124(8). http://dx.doi.org/10.1161/circresaha.118.313889.

[3] Leung CM, de Haan P, Ronaldson-Bouchard K, Kim G-A, Ko J, Rho HS, Chen Z, Habibovic P, Jeon NL, Takayama S, Shuler ML, Vunjak-Novakovic G, Frey O, Verpoorte E, Toh Y-C. A guide to the organ-on-a-chip. Nat Rev Methods Prim 2022;2(1). http://dx.doi.org/10.1038/s43586-022-00118-6.

[4] Park J, Lee Y, Cho S, Choe A, Yeom J, Ro YG, Kim J, Kang DH, Lee S, Ko H. Soft sensors and actuators for wearable human-machine interfaces. Chem Rev 2024;124(4):1464–534. http://dx.doi.org/10.1021/acs.chemrev.3c00356.

[5] Gent AN. A new constitutive relation for rubber. Rubber Chem Technol 1996;69(1):59–61. http://dx.doi.org/10.5254/1.3538357.

[6] Yeoh OH. Characterization of elastic properties of carbon-black-filled rubber vulcanizates. Rubber Chem Technol 1990;63(5):792–805. http://dx.doi.org/10.5254/1.3538289.

[7] Zhao F. Continuum constitutive modeling for isotropic hyperelastic materials. Adv Pure Math 2016;06(09):571–82. http://dx.doi.org/10.4236/apm.2016.69046.

[8] Kuhl E, Goriely A. I too I2: A new class of hyperelastic isotropic incompressible models based solely on the second invariant. J Mech Phys Solids 2024;188. http://dx.doi.org/10.1016/j.jmps.2024.105670.

[9] Bustamante R, Rajagopal KR. A new type of constitutive equation for nonlinear elastic bodies. fitting with experimental data for rubber-like materials. Proc R Soc A: Math Phys Eng Sci 2021;477(2252). http://dx.doi.org/10.1098/rspa.2021.0330.

[10] Melly SK, Liu L, Liu Y, Leng J. A phenomenological constitutive model for predicting both the moderate and large deformation behavior of elastomeric materials. Mech Mater 2022;165. http://dx.doi.org/10.1016/j.mechmat.2021.104179.

[11] Flory PJ, Rehner J. Statistical mechanics of cross-linked polymer networks I. Rubberlike elasticity. J Chem Phys 1943;11(11):512–20. http://dx.doi.org/10.1063/1.1723791.

[12] Treloar LRG. The elasticity of a network of long-chain molecules.—III. Trans Faraday Soc 1946;42:83–94. http://dx.doi.org/10.1039/TF9464200083.

[13] Arruda EM, Boyce MC. A three-dimensional constitutive model for the large stretch behavior of rubber elastic materials. J Mech Phys Solids 1993;41(2):389–412. http://dx.doi.org/10.1016/0022-5096(93)90013-6.

[14] Wu PD, Van Der Giessen E. On improved network models for rubber elasticity and their applications to orientation hardening in glassy polymers. J Mech Phys Solids 1993;41(3):427–56. http://dx.doi.org/10.1016/0022-5096(93)90043-F.

[15] Edwards SF, Vilgis T. The effect of entanglements in rubber elasticity. Polymer 1986;27(4):483–92. http://dx.doi.org/10.1016/0032-3861(86)90231-4.

[16] Edwards SF, Vilgis TA. The tube model theory of rubber elasticity. Rep Progr Phys 1988;51(2):243. http://dx.doi.org/10.1088/0034-4885/51/2/003.

[17] Beatty MF. An average-stretch full-network model for rubber elasticity. J Elasticity 2003;70(1–3):65–86. http://dx.doi.org/10.1023/B:ELAS.0000005553.38563.91.

[18] Bechir H, Chevalier L, Idjeri M. A three-dimensional network model for rubber elasticity: The effect of local entanglements constraints. Internat J Engrg Sci 2010;48(3):265–74. http://dx.doi.org/10.1016/j.ijengsci.2009.10.004.

[19] Miehe C, Göktepe S, Lulei F. A micro-macro approach to rubber-like materials -: Part I:: the non-affine micro-sphere model of rubber elasticity. J Mech Phys Solids 2004;52(11):2617–60. http://dx.doi.org/10.1016/j.jmps.2004.03.011.

[20] Miehe C, Göktepe S. A micro–macro approach to rubber-like materials. Part II: The micro-sphere model of finite rubber viscoelasticity. J Mech Phys Solids 2005;53(10):2231–58. http://dx.doi.org/10.1016/j.jmps.2005.04.006.

[21] Treloar LRG, Riding G, Gee G. A non-Gaussian theory for rubber in biaxial strain. I. Mechanical properties. Proc R Soc A 1979;369(1737):261–80. http://dx.doi.org/10.1098/rspa.1979.0163.

[22] Marckmann G, Verron E. Comparison of hyperelastic models for rubber-like materials. Rubber Chem Technol 2006;79(5):835–58. http://dx.doi.org/10.5254/1.3547969.

[23] Dal H, Açıkgöz K, Badienia Y. On the performance of isotropic hyperelastic constitutive models for rubber-like materials: A state of the art review. Appl Mech Rev 2021;73(2). http://dx.doi.org/10.1115/1.4050978.

[24] He H, Zhang Q, Zhang Y, Chen J, Zhang L, Li F. A comparative study of 85 hyperelastic constitutive models for both unfilled rubber and highly filled rubber nanocomposite material. Nano Mater Sci 2022;4(2):64–82. http://dx.doi.org/10.1016/j.nanoms.2021.07.003.

[25] Ricker A, Wriggers P. Systematic fitting and comparison of hyperelastic continuum models for elastomers. Arch Comput Methods Eng 2023;30(3):2257–88. http://dx.doi.org/10.1007/s11831-022-09865-x.

[26] Diani J, Le Tallec P. A fully equilibrated microsphere model with damage for rubberlike materials. J Mech Phys Solids 2019;124:702–13. http://dx.doi.org/10.1016/j.jmps.2018.11.021.

[27] Xiao R, Mai T-T, Urayama K, Gong JP, Qu S. Micromechanical modeling of the multi-axial deformation behavior in double network hydrogels. Int J Plast 2021;137. http://dx.doi.org/10.1016/j.ijplas.2020.102901.

[28] Zhan L, Wang S, Qu S, Steinmann P, Xiao R. A general continuum damage model for soft composites. J Mech Phys Solids 2023;175. http://dx.doi.org/10.1016/j.jmps.2023.105290.

[29] Ostwald R, Bartel T, Menzel A. A computational micro-sphere model applied to the simulation of phase-transformations. ZAMM - J Appl Math Mech / Z Für Angew Math Und Mech 2010;90(7–8):605–22. http://dx.doi.org/10.1002/zamm.200900390.

[30] Verron E, Gros A. An equal force theory for network models of soft materials with arbitrary molecular weight distribution. J Mech Phys Solids 2017;106:176–90. http://dx.doi.org/10.1016/j.jmps.2017.05.018.

[31] Okumura K. Toughness of double elastic networks. Europhys Lett 2004;67(3):470–6. http://dx.doi.org/10.1209/epl/i2003-10292-x.

[32] Nian G, Kim J, Bao X, Suo Z. Making highly elastic and tough hydrogels from doughs. Adv Mater 2022;34(50):e2206577. http://dx.doi.org/10.1002/adma.202206577.

[33] Zhong D, Wang Z, Xu J, Liu J, Xiao R, Qu S, Yang W. A strategy for tough and fatigue-resistant hydrogels via loose cross-linking and dense dehydration-induced entanglements. Nat Commun 2024;15(1):5896. http://dx.doi.org/10.1038/s41467-024-50364-3.

[34] Zhu R, Zhu D, Zheng Z, Wang X. Tough double network hydrogels with rapid self-reinforcement and low hysteresis based on highly entangled networks. Nat Commun 2024;15(1):1344. http://dx.doi.org/10.1038/s41467-024-45485-8.

[35] Wang F-S, Kosovsky LM, Krist EC, Kruse BJ, Zhukhovitskiy AV. Trapped entanglements in polymer networks: formation and characterization. Trends Chem 2024;6(8):447–58. http://dx.doi.org/10.1016/j.trechm.2024.05.005.

[36] Dhand AP, Davidson MD, Zlotnick HM, Kolibaba TJ, Killgore JP, Burdick JA. Additive manufacturing of highly entangled polymer networks. Science 2024;385(6708):566–72. http://dx.doi.org/10.1126/science.adn6925.

[37] Edwards SF. Statistical mechanics with topological constraints: I. Proc Phys Soc 1967;91(3):513–9. http://dx.doi.org/10.1088/0370-1328/91/3/301.

[38] Heinrich G, Kaliske M. Theoretical and numerical formulation of a molecular based constitutive tube-model of rubber elasticity. Comput Theor Polym Sci 1997;7(3):227–41. http://dx.doi.org/10.1016/S1089-3156(98)00010-5.

[39] Rubinstein M, Panyukov S. Nonaffine deformation and elasticity of polymer networks. Macromolecules 1997;30(25):8036–44. http://dx.doi.org/10.1021/ma970364k.

[40] Mergell B, Everaers R. Tube models for rubber-elastic systems. Macromolecules 2001;34(16):5675–86. http://dx.doi.org/10.1021/ma002228c.

[41] Darabi E, Itskov M. A generalized tube model of rubber elasticity. Soft Matter 2021;17(6):1675–84. http://dx.doi.org/10.1039/d0sm02055a.

[42] Xiang Y, Zhong D, Rudykh S, Zhou H, Qu S, Yang W. A review of physically based and thermodynamically based constitutive models for soft materials. J Appl Mech 2020;87(11). http://dx.doi.org/10.1115/1.4047776.

[43] Kaliske M, Heinrich G. An extended tube-model for rubber elasticity: Statistical-mechanical theory and finite element implementation. Rubber Chem Technol 1999;72(4):602–32. http://dx.doi.org/10.5254/1.3538822.

[44] Xiang Y, Zhong D, Wang P, Mao G, Yu H, Qu S. A general constitutive model of soft elastomers. J Mech Phys Solids 2018;117:110–22. http://dx.doi.org/10.1016/j.jmps.2018.04.016.

[45] Xiang Y, Zhong D, Wang P, Yin T, Zhou H, Yu H, Baliga C, Qu S, Yang W. A physically based visco-hyperelastic constitutive model for soft materials. J Mech Phys Solids 2019;128:208–18. http://dx.doi.org/10.1016/j.jmps.2019.04.010.

[46] Wang MC, Guth E. Statistical theory of networks of non-Gaussian flexible chains. J Chem Phys 1952;20(7):1144–57. http://dx.doi.org/10.1063/1.1700682.

[47] Xing Z, Wang X, Hu X, Zhao R. A multi-well energy landscape strategy of the rubber-like polymers undergoing intermolecular interactions for exploring rubber elasticity. Internat J Engrg Sci 2026;220. http://dx.doi.org/10.1016/j.ijengsci.2025.104438.

[48] Valanis KC, Landel RF. The strain-energy function of a hyperelastic material in terms of the extension ratios. J Appl Phys 1967;38(7):2997–3002. http://dx.doi.org/10.1063/1.1710039.

[49] Valanis KC. The valanis–landel strain energy function elasticity of incompressible and compressible rubber-like materials. Int J Solids Struct 2022;238. http://dx.doi.org/10.1016/j.ijsolstr.2021.111271.

[50] Ogden RW. Large deformation isotropic elasticity – on the correlation of theory and experiment for incompressible rubberlike solids. Proc R Soc A 1972;326(1567):565–84. http://dx.doi.org/10.1098/rspa.1972.0026.

[51] Rivlin RS. Large elastic deformations of isotropic materials iv. further developments of the general theory. Philos Trans R Soc Lond Ser A: Math Phys Sci 1948;241(835):379–97. http://dx.doi.org/10.1098/rsta.1948.0024.

[52] Rivlin RS, Sawyers KN. The strain-energy function for elastomers. Trans Soc Rheol 1976;20(4):545–57. http://dx.doi.org/10.1122/1.549436.

[53] Lopez-Pamies O. A new I1-based hyperelastic model for rubber elastic materials. Comptes Rendus. Mécanique 2009;338(1):3–11. http://dx.doi.org/10.1016/j.crme.2009.12.007.

[54] Horgan CO, Saccomandi G. A molecular-statistical basis for the gent constitutive model of rubber elasticity. J Elasticity 2002;68(1):167–76. http://dx.doi.org/10.1023/A:1026029111723.

[55] Horgan CO. The remarkable gent constitutive model for hyperelastic materials. Int J Non-Linear Mech 2015;68:9–16. http://dx.doi.org/10.1016/j.ijnonlinmec.2014.05.010.

[56] Puglisi G, Saccomandi G. Multi-scale modelling of rubber-like materials and soft tissues: an appraisal. Proc Math Phys Eng Sci 2016;472(2187):20160060. http://dx.doi.org/10.1098/rspa.2016.0060.

[57] Anssari-Benam A, Bucchi A. A generalised neo-hookean strain energy function for application to the finite deformation of elastomers. Int J Non-Linear Mech 2021;128. http://dx.doi.org/10.1016/j.ijnonlinmec.2020.103626.

[58] Anssari-Benam A, Horgan CO. A three-parameter structurally motivated robust constitutive model for isotropic incompressible unfilled and filled rubber-like materials. Eur J Mech A Solids 2022;95. http://dx.doi.org/10.1016/j.euromechsol.2022.104605.

[59] Anssari-Benam A. On a new class of non-Gaussian molecular-based constitutive models with limiting chain extensibility for incompressible rubber-like materials. Math Mech Solids 2021;26(11):1660–74. http://dx.doi.org/10.1177/10812865211001094.

[60] Pucci E, Saccomandi G. A note on the gent model for rubber-like materials. Rubber Chem Technol 2002;75(5):839–52. http://dx.doi.org/10.5254/1.3547687.

[61] Anssari-Benam A. Large isotropic elastic deformations: On a comprehensive model to correlate the theory and experiments for incompressible rubber-like materials. J Elasticity 2023;153(2):219–44. http://dx.doi.org/10.1007/s10659-022-09982-5.

[62] Anssari-Benam A, Goriely A, Saccomandi G. Generalised invariants and pseudo-universal relationships for hyperelastic materials: A new approach to constitutive modelling. J Mech Phys Solids 2024;193. http://dx.doi.org/10.1016/j.jmps.2024.105883.

[63] Martonová D, Goriely A, Kuhl E. Generalized invariants meet constitutive neural networks: A novel framework for hyperelastic materials. J Mech Phys Solids 2026;206. http://dx.doi.org/10.1016/j.jmps.2025.106352.

[64] Anssari-Benam A, Saccomandi G. Large isotropic elastic deformations: On a comprehensive model to correlate the theory and experiments for compressible rubber-like materials. J Elasticity 2025;157(2). http://dx.doi.org/10.1007/s10659-025-10122-y.

[65] Guan J, Li X, Yuan H, Liu J. Hyperelastic modeling based on generalized Landau invariants and multi-stage calibration. J Mech Phys Solids 2026;206. http://dx.doi.org/10.1016/j.jmps.2025.106338.

[66] Kuhn W, Grün F. Beziehungen zwischen elastischen konstanten und dehnungsdoppelbrechung hochelastischer stoffe. Kolloid-Zeitschrift 1942;101(3):248–71. http://dx.doi.org/10.1007/BF01793684.

[67] Moosavian H, Tang T. A critical examination of force–extension relationship for freely jointed chain model. Extrem Mech Lett 2023;60. http://dx.doi.org/10.1016/j.eml.2023.101987.

[68] Eaton ML. On the projections of isotropic distributions. Ann Statist 1981;9(2):391–400.

[69] Dal H, Gültekin O, Açıkgöz K. An extended eight-chain model for hyperelastic and finite viscoelastic response of rubberlike materials: Theory, experiments and numerical aspects. J Mech Phys Solids 2020;145. http://dx.doi.org/10.1016/j.jmps.2020.104159.

[70] Liu Y, Zhang H, Zhang J, Zheng Y. Constitutive modeling for polymer hydrogels: A new perspective and applications to anisotropic hydrogels in free swelling. Eur J Mech A Solids 2015;54:171–86. http://dx.doi.org/10.1016/j.euromechsol.2015.07.001.

[71] Davidson JD, Goulbourne NC. A nonaffine network model for elastomers undergoing finite deformations. J Mech Phys Solids 2013;61(8):1784–97. http://dx.doi.org/10.1016/j.jmps.2013.03.009.

[72] Finkelmann H, Greve A, Warner M. The elastic anisotropy of nematic elastomers. Eur Phys J E 2001;5(3):281–93. http://dx.doi.org/10.1007/s101890170060.

[73] Hirschmann H, Roberts PMS, Davis FJ, Guo W, Hasson CD, Mitchell GR. Liquid crystalline elastomers: the relationship between macroscopic behaviour and the level of backbone anisotropy. Polymer 2001;42(16):7063–71. http://dx.doi.org/10.1016/S0032-3861(01)00135-5.

[74] Lamont SC, Vernerey FJ. Generalized continuum theory for nematic elastomers: Non-affine motion and characteristic behavior. J Mech Phys Solids 2024;190. http://dx.doi.org/10.1016/j.jmps.2024.105718.

[75] Edwards SF. The statistical mechanics of polymerized material. Proc Phys Soc 1967;92(1):9. http://dx.doi.org/10.1088/0370-1328/92/1/303.

[76] Kröger M. Simple, admissible, and accurate approximants of the inverse langevin and brillouin functions, relevant for strong polymer deformations and flows. J Non-Newton Fluid Mech 2015;223:77–87. http://dx.doi.org/10.1016/j.jnnfm.2015.05.007.

[77] Carniel EL. Generalized incremental moduli of hyperelastic materials. J Appl Mech 2025;92(11). http://dx.doi.org/10.1115/1.4069072.

[78] Carniel EL. Characterization of strain-induced anisotropy in isotropic hyperelastic materials via generalized incremental moduli. Int J Mech Sci 2026;310. http://dx.doi.org/10.1016/j.ijmecsci.2025.111076.

[79] Treloar LRG. Stress-strain data for vulcanised rubber under various types of deformation. Trans Faraday Soc 1944;40:59–70. http://dx.doi.org/10.1039/TF9444000059.

[80] Jones DF, Treloar LRG. The properties of rubber in pure homogeneous strain. J Phys D: Appl Phys 1975;8(11):1285. http://dx.doi.org/10.1088/0022-3727/8/11/007.

[81] Katashima T, Urayama K, Chung U-i, Sakai T. Strain energy density function of a near-ideal polymer network estimated by biaxial deformation of tetra-PEG gel. Soft Matter 2012;8(31). http://dx.doi.org/10.1039/c2sm25340b.

[82] Kawabata S, Matsuda M, Tei K, Kawai H. Experimental survey of the strain energy density function of isoprene rubber vulcanizate. Macromolecules 1981;14(1):154–62. http://dx.doi.org/10.1021/ma50002a032.

[83] Zhan L, Wang S, Qu S, Steinmann P, Xiao R. A new micro–macro transition for hyperelastic materials. J Mech Phys Solids 2023;171. http://dx.doi.org/10.1016/j.jmps.2022.105156.

[84] Neff P, Ghiba I-D, Lankeit J. The exponentiated hencky-logarithmic strain energy. Part I: Constitutive issues and rank-one convexity. J Elasticity 2015;121(2):143–234. http://dx.doi.org/10.1007/s10659-015-9524-7.

[85] Shi H, Yan Z, Shi J, Yang Z, Gao Y, Xu J, Liu Z. Tuning the stiffness and stretchability of micro-scale-structured polymer membrane simultaneously by integrating mechanical modeling and spatiotemporal controllable photolithograph. J Mech Phys Solids 2024;193. http://dx.doi.org/10.1016/j.jmps.2024.105906.

[86] Bahrololoumi A, Mohammadi H, Moravati V, Dargazany R. A physically-based model for thermo-oxidative and hydrolytic aging of elastomers. Int J Mech Sci 2021;194. http://dx.doi.org/10.1016/j.ijmecsci.2020.106193.

[87] Liao JG, Berg A. Sharpening jensen's inequality. Amer Statist 2018;73(3):278–81. http://dx.doi.org/10.1080/00031305.2017.1419145.

[88] Lee SK, Chang JH, Kim H-M. Further sharpening of jensen's inequality. Statistics 2021;55(5):1154–68. http://dx.doi.org/10.1080/02331888.2021.1998052.

[89] Agahi H. On Jensen's gap by Taylor's theorem. Math Methods Appl Sci 2021;44(14):11565–70. http://dx.doi.org/10.1002/mma.7514.

[90] Lei J, Liu Z. A network mechanics method to study the mechanism of the large-deformation fracture of elastomers. J Appl Phys 2022;132(13). http://dx.doi.org/10.1063/5.0106445.

[91] You H, Zheng S, Li H. A network graph entropy-based general model for soft polymer networks. Int J Mech Sci 2025;305. http://dx.doi.org/10.1016/j.ijmecsci.2025.110732.

[92] Yang J, Chen K, Yu C, Zhou K, Kang G. A hyperelastic constitutive model for soft elastomers considering the entanglement-dependent finite extensibility. J Mech Phys Solids 2025;196. http://dx.doi.org/10.1016/j.jmps.2024.106000.

[93] Buche MR, Silberstein MN, Grutzik SJ. Freely jointed chain models with extensible links. Phys Rev E 2022;106(2–1):024502. http://dx.doi.org/10.1103/PhysRevE.106.024502.

[94] Mulderrig J, Talamini B, Bouklas N. A statistical mechanics framework for polymer chain scission, based on the concepts of distorted bond potential and asymptotic matching. J Mech Phys Solids 2023;174. http://dx.doi.org/10.1016/j.jmps.2023.105244.

[95] Marsaglia G. Choosing a point from the surface of a sphere. Ann Math Stat 1972;43(2):645–6, 2. http://dx.doi.org/10.1214/aoms/1177692644.